Taylor & Francis
Taylor & Francis Group

Mechanics of Advanced Materials and Structures

ISSN: (Print) (Online) Journal homepage: www.tandfonline.com/journals/umcm20

Development of high-performance nanostructured aluminum and its constitutive modeling

Surja Deka, Farzin Mozafari, Ashis Mallick, Prakash Thamburaja & Manoj Gupta

To cite this article: Surja Deka, Farzin Mozafari, Ashis Mallick, Prakash Thamburaja & Manoj Gupta (11 Oct 2023): Development of high-performance nanostructured aluminum and its constitutive modeling, Mechanics of Advanced Materials and Structures, DOI: 10.1080/15376494.2023.2262733

To link to this article: https://doi.org/10.1080/15376494.2023.2262733

MECHANICS OF ADVANCED MATERIALS AND STRUCTURES
https://doi.org/10.1080/15376494.2023.2262733

ORIGINAL ARTICLE

Development of high-performance nanostructured aluminum and its constitutive modeling

Surja Deka[a], Farzin Mozafari[b], Ashis Mallick[a], Prakash Thamburaja[c,d], and Manoj Gupta[e]

[a]Department of Mechanical Engineering, Indian institute of Technology (ISM) Dhanbad, Dhanbad, Jharkhand, India; [b]Department of Mechanical Engineering, Abdullah Gül University, Kayseri, Turkey; [c]Department of Mechanical and Manufacturing Engineering, National University of Malaysia (UKM), Bangi, Selangor, Malaysia; [d]Department of Mechanical Engineering, Texas A & M University, College Station, Texas, USA; [e]Department of Mechanical Engineering, National University of Singapore, Singapore, Singapore

ABSTRACT

A new technique, an in-situ hot-extrusion-based synthesizing process, is proposed to develop high-performance nanocrystalline aluminum (nc-Al) with an optimally tuned strength-to-ductility ratio suitable for various technologically relevant applications. Comprehensive investigations are conducted by characterizing mechanical and microstructural properties to realize the influence of various synthesizing variables on the properties of the bulk nc-Al. Furthermore, a continuum-scale constitutive modeling approach is proposed based on dominant microstructural mechanisms of plastic deformation and implemented into a finite element solver using a user-defined material interface. It is shown that the proposed theory can provide a versatile platform to predict the nanocrystalline aluminum mechanical response quite well.

ARTICLE HISTORY
Received 21 December 2022
Accepted 31 May 2023

KEYWORDS
Nanocrystalline metal; high-energy ball milling; constitutive model; finite element analysis; mechanical properties

1. Introduction

Nanostructured metals characterized by ultrafine crystalline grains in the order of nanometers (i.e. $\leq 100\,\mathrm{nm}$) have received much attention in recent years due to their outstanding mechanical properties [1,2]. However, nanostructured materials' practical excellence is vitally dependent on reaching an optimal compromise between strength and ductility [3]. This is because there is competition between the intragrain mechanical responses versus the grain boundary region mechanical response in nanocrystalline materials since the volume occupied by the grain boundary region in nanocrystalline materials is sizeable [4]. In addition, numerical studies have shown that i) loading history also influences the properties of nanocrystalline materials [5], and (ii) the interaction between nanotwins and dislocation pileups influences the toughening mechanisms in nanomaterials [2], and these effects further add to the complexity of fully-understanding the nature of these materials.

Recently, aluminum-based nanostructured materials have been widely used in many engineering fields, such as the aerospace and automobile industries [6]. This is due to its versatility, high specific strength, lightweightness and excellent corrosion resistance. However, there are some challenges to the frequent use of aluminum-based nanomaterials in components and structures, namely that these materials are difficult to produce due to the inherent tendency of the material to exhibit a coarse grain structure during consolidation [7]. Therefore, there remains a need for a low-complexity and efficient method to produce and characterize aluminum-based nanostructured materials, and the different types of synthesizing processes for these materials will be covered in detail in the following section.

1.1. A brief overview of current synthesizing processes

In recent years, numerous studies have targeted the development of nanostructured aluminum alloys, focusing on enhancing mechanical characteristics [7,8]. In a broad sense, available methodologies used for the synthesis of nanostructured aluminum can be classified into two categories, those that employ severe plastic deformation (SPD) processes such as high-pressure torsion (HPT), equal channel angular pressing (ECAP) and accumulation roll bonding (ARB), and those that include powder metallurgy technology [6,8,9]. The concept of HPT involves the concurrent application of extremely high pressure and torsional shear strain to the samples, leading to severe plastic deformation and, consequently, the formation of ultrafine-grained structures. Recently, Nurislamova et al. [10] have demonstrated that although employing the HPT technique significantly increases the mechanical strength and hardness of the Al alloy, the ductility of the synthesized samples is still not desirable for structural applications. In this regard, Orlov et al. [11] have also reported an enhancement in the ductility of nanostructured Al-Cu-Zr samples fabricated using the HPT process, while the mechanical strength of the material remains the same. According to an investigation by Oh et al. [12] the HPT-processed Al 7075 alloy exhibits a significant

CONTACT Ashis Mallick ✉ mallick@iitism.ac.in; mal123_us@yahoo.com Department of Mechanical Engineering, Indian institute of Technology (ISM) Dhanbad, Dhanbad, Jharkhand 826004, India.

improvement in its mechanical properties at elevated temperatures. Moreover, the study has emphasized the correlation between the dynamic precipitation and mechanical strength of HPT-processed Al alloys. Despite these advantages, the HPT usually delivers small synthesized material samples that are mainly not useful for meaningful mechanical testing and practical usage. Furthermore, although the HPT process is widely studied in the context of nanostructured and ultrafine sample production and dramatically enhances the materials' mechanical properties, the intrinsic inhomogeneity in torsion-induced deformation implies significant limitations to fabricating macroscale samples suitable for structural applications. Other severe plastic deformation processes, such as ECAP and ARB, exhibit more potential for industrialization by attracting more attention. In the ECAP process, a billet is pushed through a die having two interconnecting pathways with an abrupt angle [13]. As the sample passes through the intersection of two channels, it undergoes severe plastic deformation. The process can be repeated to achieve a desirable grain refinement, significantly improving the material's mechanical properties. Recent studies by Khelfa et al. [14] and Tanski et al. [15] illustrate a substantial increase in the hardness of nanostructured aluminum alloy fabricated using the ECAP technique, and it can be attributed to the grain refinement induced by this approach. Several further studies have examined the enhancement of the mechanical properties of Al-based nanostructured materials synthesized using the ECAP process [16–18]. However, the ECAP process, while improving samples' strength, might not be completely successful in achieving nanocrystalline structure with grain sizes less than 100 nm. Furthermore, as highlighted by Alvand et al. [19], ECAP and HPT processes yield poor quantitative productivity in terms of the capability for sample productions.

Among different SPD techniques for producing bulk nanostructured materials, ARB is the most promising one with the potential to produce large bulk materials for practical applications [19]. The primary aim of the ARB is to impose a high amount of plastic deformation on the material, resulting in microstructural refinement and thereby increasing the material's strength without altering the material dimensions [20]. The study by Morovvati and Dariani [20] has comprehensively investigated the nanostructured Al 1100 processed *via* the ARB process from experimental, analytical, and numerical perspectives. Here, significant mechanical strength and hardness enhancements have been observed because of the microstructure refinement brought out by the ARB process and the formation of the brittle intermetallic compounds at the interfaces [20,21]. Yu et al. [22] made similar observations about the mechanical properties of nanostructured Al 1050 sheets. The study has augmented the material's tensile properties threefold and reported a marked increase in the hardness of the material, while improvements are not significant in the preheated state. As a less-noticed and cost-effective SPD technique for producing ultrafine and nanoscale material, friction welding is also notable, wherein a rotational shearing force is added to the linear extrusion. Due to its intrinsic nature of producing a refined microstructure, it enhances the mechanical properties significantly, see [3,23–25]. In general, the SPD process involves the application of large strains to the material to achieve a highly refined grain structure that is mainly free of porosity and contamination [26]. However, the SPD process does not efficiently yield specifically desired material properties and uniform refined structures. Moreover, requiring precise fabrication setup, built-in complexity of the process, and high production cost strongly limits the interest in these techniques [26]. Hence, to tackle the issues raised, powder metallurgy technology provides a suitable alternative for the production of various alloys and tailor-made microstructures. As noticed by Salur et al. [27] powder metallurgy techniques, while alleviating the undesirable internal interactions of the material, can favorably fabricate samples with the end-use size and shape without requiring any secondary machining process such as turning, drilling, and milling.

The treatment of powder metallurgy processes within the context of the development of nanostructured aluminum alloys has been addressed in several contributions. Recently, Kushwaha et al. [6] has employed a spark plasma-assisted cryogenic milling process to synthesize nc-Al. Here, although the effects of cryomilling on the microstructural and mechanical behavior have been profoundly investigated, the characterization of the mechanical properties has been restricted to hardness tests. Liu et al. [28] have also shown that nc-Al produced by spark plasma-assisted cryogenic milling exhibits a significant improvement in mechanical properties over its coarse-grained counterpart. The study also highlighted the need to apply lower sintering temperatures and higher holding pressure to restrain grain growth and consequently enhance mechanical properties. In another study, Christudasjustus et al. [29] utilized a plasma-assisted ball milling process at room temperature to synthesize nanocrystalline Al-xV alloys. Here, by exploring the influence of SPS temperature on the elastic modulus and hardness, it is concluded that the hardness and elastic modulus of Al-xV alloys could be noticeably higher than commercial Al alloys due to the better solubility of the V within Al. Vidyasagar, and Karunakar [30] have further adopted similar processes to fabricate an Al-based alloy composite for providing an in-depth analysis of the material's mechanical properties in relation to its micro and nanostructures. The formation of nano and ultrafine grain due to Joule's heating and thermomechanical fatigue, along with the formation of the precipitates, explains the improved mechanical properties of the material. However, a clear understanding of the kinematics of the precipitates, which could have led to a profound insight into the enhancement of the mechanical properties, is missed. Please refer to [7,31,32] for more details on the materials' mechanical properties synthesized using the cryogenic milling process. In this regard, Tang et al. [33] have also provided a thorough discussion on the mechanical properties of the nanostructured Al alloy synthesized by cryogenic milling followed by the hot extrusion process. For convenience, we present a summary of the most commonly used synthesizing processes in Table 1, but this list is not an exhaustive list.

Table 1. Summary of current synthesizing processes for nanostructured aluminum.

Synthesizing process	References
High pressure torsion	Latynina et al. [34], Nurislamova et al. [10], Orlov et al. [11], Oh et al. [12]
Equal channel angular pressing	Agarwal et al. [13], Khelfa et al. [14], Tański et al. [15], May et al. [16], Su et al. [17], Sabirov et al. [18]
Accumulative roll-bonding	Alvand et al. [19], Morovvati, and Dariani [20], Böhner et al. [21], Yu et al. [22]
Friction extrusion	Whalen et al. [3], Su et al. [23], Ma et al. [24], Su et al. [25]
Cryogenic milling + Spark plasma sintering	Kushwaha et al. [6], Liu et al. [28], Borse et al. [35], Kushwaha et al. [36]
Ball milling + Spark plasma sintering	Rana et al. [7], Christudasjustus et al. [29], Vidyasagar, and Karunakar [30], Cao et al. [37]
Cryogenic milling + Hot extrusion	Han, and Lavernia [31], Hayes et al. [32], Tang et al. [33], Han et al. [38]

1.2. The proposed synthesizing process

The present synthesizing process effectively utilizes the powder metallurgy technique to overcome shortcomings of the current fabrication processes for developing high performance nanostructured aluminum. It is important to reiterate that the powder metallurgy technique is ideal for making near-net shape parts of complex geometries from various materials, thus optimizing the material utilization and minimizing the secondary machining operations. The proposed synthesizing process to produce nanostructured aluminum material comprises powder milling, compaction, and sintering, followed by hot extrusion. The high-energy ball milling process is adopted to reduce the crystallite size of the powder particles to obtain the desired microstructure. High energy ball milling introduces severe plastic deformation while milling the powder and thus produces a high density of dislocations. This, in turn, along with the introduction of high-strain energy, the recovery and recrystallization facilitates the reduction of the crystalline coherence zone and reduces the size of the crystallite [39]. Another important aspect during high energy ball milling is the milling time, which has a direct relation with the powder morphology and particle size. Thus, it plays a vital role in obtaining the desired microstructure. Special emphasis should be given to determining the milling time in the most accurate manner possible. The effectiveness of the ball milling process on crystallite size reduction has been well-recognized in several earlier studies [37,40]. Next, the milled powder is then compacted, which allows for achieving the maximum possible density for the sample. Attaining the maximum possible density ensures the minimal presence of pores and voids in the sample. The compacted samples then undergo the sintering process with the intention of developing metallurgical bonding between particles, which significantly reduces the percentage of voids and pores [41]. Finally, the billet is consolidated *via* rapid hot extrusion to produce the final extruded rod. In this regard, the work of Choi et al. [40] is noteworthy, wherein the study has posited that the hot extrusion of the milled powder enabled the production of bulk nanostructured aluminum confirmed by the TEM investigation. Despite enhancing the nanocrystalline Al's mechanical strength, the study has reported a very low degree of ductility. It is commonly believed that the low ductility of the nanostructured material will lead to a decrease in reliability and limit the material's engineering applications. Moreover, it is recommended that further research be undertaken in the areas such as investigating the rate deformation behavior concerning both compression and tension to understand the effect of the microstructural changes on the mechanical behavior of nanocrystalline aluminum. Recently, Hua et al. [42] fabricated a nanostructured $B_4C/SiC/Al$ nanocomposite following the same synthesizing procedure. Here, the aim is to synergistically strengthen the mechanical properties of $B_4C/SiC/Al$ composites based on the reinforcement particles. There is, however, a lack of understanding regarding the correlation between mechanical alloying parameters, the consolidation process, powder behavior, and bulk mechanical characteristics. Researchers can refer to the following studies concerning the synthesis of bulk nanocrystalline materials using the proposed powder metallurgy method and successive consolidation at high temperatures and its correlation with mechanical properties [43–45]. In general, as observed from prior studies, fabricating and improving the mechanical properties of ultrafine and nanostructured materials has been one of the major interesting research subjects due to its major applications in the structural, automobile, energy, electronic, and aerospace industry. Although there was much research about the tremendous improvement of mechanical properties of these ultrafine and nanostructured materials produced by SPD and powder metallurgy techniques as mentioned in Section 1.1 and Section 1.2, there has been little discussion about the optimum correlation between tensile strength and ductility. Moreover, to our knowledge, no research has been carried out on fundamental mechanisms, powder morphologies during milling, microstructure formation, structure-property, and failure mechanisms to facilitate our understanding of these aspects.

In parallel to experimental contributions, there is a great tendency toward using theoretical and computational approaches to describe the mechanical response of nanostructured aluminum alloys. Several studies have attempted to provide a theoretical framework for nanostructured metallic materials [46–49]. In doing so, molecular dynamics (MD) studies have been instrumental in understanding the micro mechanisms governing the inelastic deformation process of nanocrystalline materials [46,47]. In particular, the work of Yamakov et al. [46] can be emphasized, wherein they performed a molecular dynamics simulation for the deformation behavior of nc-Al. The simulation was done by considering mechanical twinning as the dominant mechanism. Later, in contrast to Yamakov et al. [46], Kadau et al. [48] performed a molecular dynamics simulation of nc-Al where they considered the sliding mechanism between the grains as the dominant mechanism when modeling the tensile behavior of nc-Al. The molecular dynamics study can predict the material's deformation behavior, as found in the experiments. These MD methods provide valuable insights into the mechanical response of materials at the atomic level. However, they are insufficient for simulations of deformation and failure under conditions similar to those in which materials are tested physically. Another major limitation of MD simulations is the simulated time, which is in the order of nanoseconds for large systems. Therefore, to design structural components, it would be helpful to form continuum-scale constitutive models that, when implemented in finite-element solution procedures, would be able to simulate the inelastic deformation and failure response of nanocrystalline materials in various length scales, see [49]. However, there have been few studies on developing continuum-scale constitutive modeling of bulk nanocrystalline aluminum. In this regard, Khan and Zhang [50] developed a continuum-based constitutive model to predict the mechanical responses of the nanocrystalline copper and iron. Later, Khan et al. [8] extended the KHL model to the nanocrystalline Al by employing a bilinear hall patch relation in the viscoplastic KHL constitutive model. However, the KHL module is greatly affected whenever the stress value exceeds the initial yield stress value. Zhan et al. [51] developed a phenomenological constitutive model to model ultrafine Al's temperature sensitivity and post-yield behavior. However, the study is not addressed the strain rate dependency and hardness characterization of nc-Al. In the last few years, Wei and Anand [52] have developed a seminal idea regarding modeling nanostructured materials on the continuum scale. Here, a phenomenological large-deformation, isotropic, rate-dependent elastic-plastic model has been developed that pressure dependency is accounted for by proposing a plastically dilatant and non-normal flow rule. The model successfully predicts the nanostructured Mg and Cu's tensile, compression, and micro-indentation responses using the physical deformation micro mechanisms. The versatility of the theory developed by Wei and Anand [52] provides the primary motivation for the present study to evaluate the application of the continuum-scale constitutive theory for understanding the mechanical performance of bulk nanocrystalline aluminum.

Therefore, the study's first aim is to develop a high-performance nanocrystalline aluminum possessing an optimized strength-to-ductility ratio suitable for various technologically relevant applications. In doing so, an in-situ hot-extrusion-based synthesizing process is proposed to fabricate bulk nc-Al samples by determining an efficient correlation between the microstructural and morphological evolution of the Al particles with the milling time. Comprehensive characterizations are conducted on the mechanical properties of nc-Al samples to identify the various parameters affecting their properties. For instance, a detailed analysis of the nc-Al samples' hardness is presented regarding its ball milling, sintering, and extrusion capability, along with a comparison with its coarse-grained counterpart. A thorough investigation is also conducted on the tensile behavior and the fracture morphology of nc-Al samples at various strain rates, which leads to a profound insight into the dominant failure mechanism of nc-Al materials. The second aim of our study is to propose a reliable modeling framework to capture the deformation behavior of bulk nc-Al materials in macroscale engineering applications. In this regard, a constitutive modeling approach is presented using a recently developed continuum-scale isotropic rate-dependent plasticity model. The proposed model is computationally implemented into Abaqus/Explicit finite element solver using an explicit-based time integration method *via* a user-defined material subroutine. The model's predictive capabilities are then examined by comparing different numerical results with experimental data obtained from compression/tensile and Vickers micro indentation experiments.

This paper is organized as follows: Section 2 outlines an in-situ hot-extrusion based synthesizing process to develop a high-performance bulk nc-Al. A comprehensive microstructural and mechanical properties characterization is made along with the synthesized nc-Al samples. Section 3 is devoted to presenting a continuum-scale constitutive modeling approach and its computational implementation to predict the mechanical response of nc-al material. An ad-hoc calibration procedure for the newly introduced constitutive material parameter is outlined. This section also explores the predictive capabilities of the present model in the context of tensile/compression and micro indentation simulations. Overall conclusions regarding the present work are provided in Section 4 together with an outlook.

2. Experimental methodology & material characterization

This section describes the raw materials and a novel in-situ hot-extrusion-based synthesizing process to fabricate bulk nanocrystalline aluminum. Moreover, it outlines material characterization methodologies employed to comprehensively investigate synthesized nc-Al samples from a microstructural and mechanical behavior perspective, including morphological & microstructural evolutions, density & micro hardness measurements, tensile, compression testing, and fracture behavior.

2.1. *In-situ hot-extrusion-based synthesizing process*

The present study proposes a novel in-situ hot-extrusion-based synthesizing process to efficiently fabricate bulk nanocrystalline aluminum, which is extensively employed in technologically relevant applications (Figure 1). In doing so, the raw material for the nanostructured aluminum synthesizing process was supplied by Sisco Research Laboratories Pvt. Ltd., India, in the form of aluminum powders with a mesh size of 325 and 99.5% purity. Figure 2 depicts the primary characterization result for as-received aluminum powder using the Supra 55 Zeiss Field Emission Scanning Electron Microscope (FESEM) taken with a magnification of 5.50 KX at 5.00 kV. It is evident from the FESEM results that the as received Al powders have predominantly elongated morphology, with a small fraction having spherical morphologies

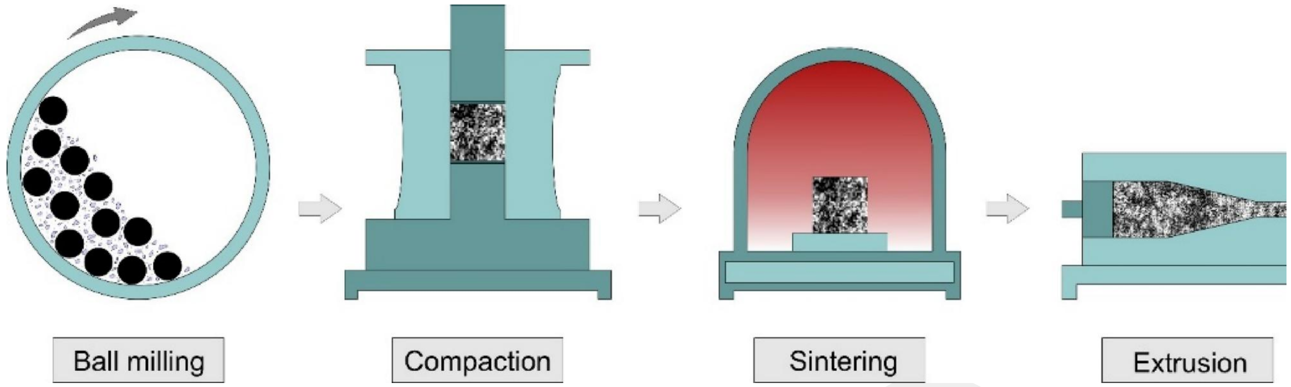

Figure 1. Schematic illustration of an in-situ hot-extrusion-based synthesizing process comprising ball milling, compaction, sintering, and extrusion.

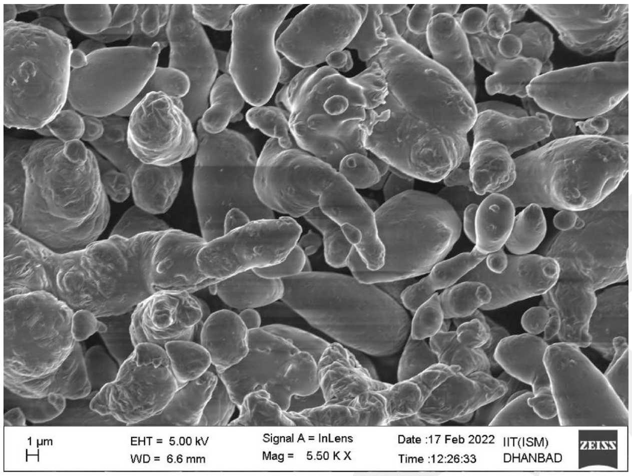

Figure 2. Primary characterization of as-received aluminum powder using Field Emission Scanning Electron Microscope (FESEM) taken at a magnification of 5.50 KX at 5.00 kV. Powders exhibit predominantly elongated morphology, with a small fraction having spherical morphologies.

and an average particle size of 11 µm. Afterward, a high energy ball milling process with a ball-to-powder ratio of 10:1 was carried out on the as received powders to reduce the crystallite size of the powder significantly. The ball milling process was conducted using balls with a diameter of 16 mm at a rotational speed of 250 rpm for various milling times from 3 to 65 h. This is to note that the 65 h milling time is taken from the work of Rijesh et al. [53], wherein they reported that the minimum crystallite size was attained between 60–65h. Furthermore, in accordance with the research of Abdoli et al. [54], we used a time increment of 5 h, post 15 h of ball milling. In the initial phase of ball milling, between 0 15 h, we used a small-time increment of 3 h to closely monitor the changes in the powder's morphology and size. It is also important to note that during the ball milling process, 1.5% stearic acid was added as the process control agent (PCA) to prevent cold welding of powder particles, as proposed by Charistudasjustus et al. [29]. Before proceeding to the next step, several powder samples were randomly collected before and after the 65-h ball milling process as coarse grained (CG) and nanocrystalline (nc) aluminum, respectively, to ensure the milling process's effectiveness in reducing powder crystallite size. Next, samples achieved the maximum possible density through a compaction process using a cylindrical die with a diameter of 36 mm and a height of 80 mm under 50 Ton press. The compaction process delivered cylindrical billets with a diameter of 35 mm and height of 45 mm that were sintered then in the tubular furnace at the temperature of 550 °C under the argon atmosphere in order to eliminate the pores and accelerate the diffusion process that leads in forming bonds between the powder particles. Finally, sintered billet samples were densified through a hot extrusion process at a temperature of 450 °C with an extrusion ratio of 20.25:1 to approach the theoretical density. The final products of the proposed synthesizing process are the cylindrical bars with a length of around 650 mm and a diameter of 8 mm, which are used to prepare samples for various characterization purposes, as will be discussed shortly.

2.2. Morphological investigations & structural evolution

To track the microstructural changes in the powder and whether there is any impurity involved during the milling period, we have conducted an X-ray diffraction (XRD) analysis of ball-milled Al powder using a Rigaku SmartLab X-ray diffractometer equipped with Cu-Kα radiation (λ = 0.154 nm) using a scanning range of 20-90° and a step size of 4°/min. From the XRD patterns of the milled powder shown in Figure 3, it is evident that with the increase in the milling time, there is a gradual broadening of peaks, which confirms the crystallographic changes in the powder from the crystalline structure to the polycrystalline form. The peak broadening and reduction of peak intensity, in turn, is a reliable index for grain size reduction in the material. Furthermore, the Williamson Hall method can be employed to approximate the crystallite size and lattice strain of the milled powders using some peak-broadening measurements. The Williamson-Hall equation can be written as [6]:

$$\beta_T \cos\theta = (4\sin\theta)\epsilon + \frac{K\lambda}{D} \tag{1}$$

where β_T, θ, and ϵ denote total broadening, Bragg's angle, and lattice strain, respectively, the quantities λ, and D define the Scherrer constant, X-ray wavelength, and crystallite size, respectively; K is the Scherrer constant, which is 0.9 for Al [28,55]. The crystallite sizes and lattice strains determined

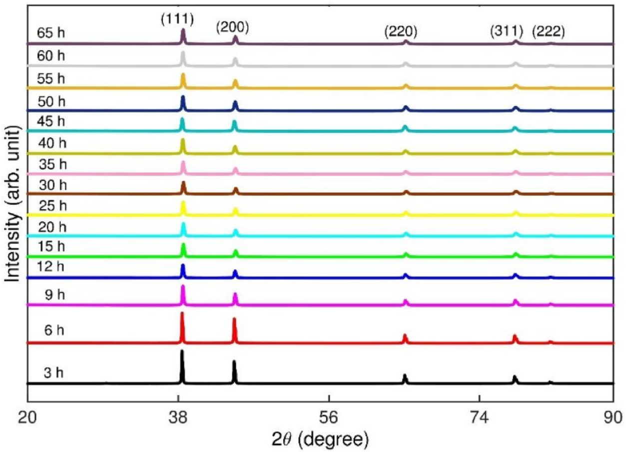

Figure 3. XRD analysis of the milled powder. The diffraction peaks are assigned to their respective miller indices, denoted by (hkl). The apparent broadening and significant reduction of the intensity of the peaks can be seen with the increase in milling time.

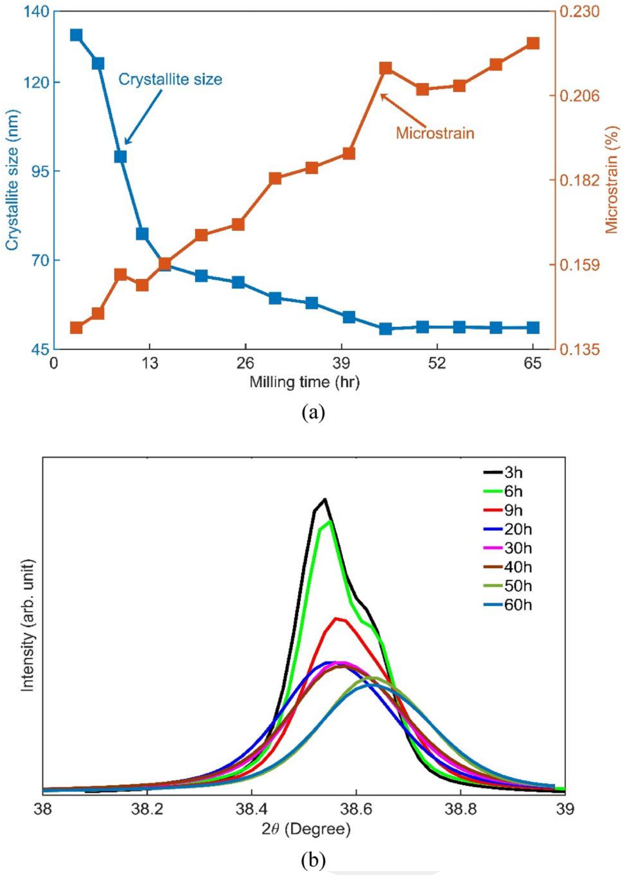

Figure 4. (a) Evolution of crystallite size and lattice microstrain of the milled Al powder with milling time, and (b) XRD diffraction pattern showing peak broadening at $2\theta = 38.6$. The shift of the principal peak (111) can be seen, which is due to the presence of stacking faults.

from the Williamson-Hall relation for different milling times are plotted in Figure 4a. From Figure 4a, it can be readily seen that increased milling time leads to a decrease in crystallite size and an increase in lattice strain. The reduction of crystallite size and the lattice strain accumulation can be attributed to the repeated impact of the balls, acting as grinding media. The powder particles deformed plastically by the shear force-dominated process followed by work hardening, which is further accompanied by cold welding and fracture of the particles. Moreover, the decrease in crystallite size can also be attributed to the formation of high dislocation density regions in the grains, stacking faults, and grain boundary pill-ups. Figure 4b demonstrates the XRD peaks plotted at $2\theta = 38.6$ for various milling times. Peak broadening along with a shift of principal peaks toward the right can be readily seen in Figure 4b that could be attributed to the stacking faults, which will be discussed shortly. It is important to note that the peak broadening at $2\theta = 38.6$ during the milling time corroborates the reduction of crystallite size, which in this case, a significant drop of about 42.11% occurs in crystallite size at the early stages of milling. Further continuation of the milling process results in a gradual reduction in the crystallite size to the lowest value of 50.6 nm at 45 h, and a non-appreciable crystallite size refinement is observed by proceeding with the milling process from 45 h. However, a slight increase in crystal size can be observed up to 65 h, which might be attributed to the effect of excessive heat generation on the crystal growth.

Figure 5 shows the evolution of particle size and powder morphology with respect to milling time. Generally, three dominant mechanisms are concerned in the mechanical alloying of the powders, including a) flattening of the powder particles, b) cold welding of powder particles, which increases the particle size, and b) eventual fracturing of the particles. In the initial phases of the milling process, the powder particles flattened by forming flakes due to the high energy imparted by balls; see Figure 5 for the details of the particle flattening and formation of flakes that occurred at milling time of 3 h to 9 h. The flattening of the particles is followed by cold welding, which in turn results in the agglomeration of particles. The cold welding of the particles is evident from the milling time of 12 h to 40 h. Following the cold welding of the particles, the fracturing mechanism of the particles activates, as can be seen in Figure 5, at the milling time of 45 h to 65 h. Particle welding, agglomeration, and fracturing can be attributed to the overwhelming ductility of aluminum and its dynamic recovery process. For the sake of clarity, Figure 6 illustrates the agglomeration and fracturing of particles at higher magnification. In Figure 6, particle fracture boundaries are specified using solid yellow lines. According to Morsi, and Esawi [56], particle welding could be extensive at higher milling times, which may pose a strong challenge during compaction and sintering. Moreover, excessive cold welding produces non-uniform microstructures and properties, which is undesirable. The study proposed adding a small percentage of process control agents (PCA) to circumvent this difficulty. Therefore, following Morsi, and Esawi [56], 0.7% of zinc stearate as a PCA was added to the milled powder at 40^{th} h in the argon gas environment to prevent excessive cold welding of the Al particles, which resulted in powder particles exhibiting flake-like morphology at 45 h of milling with a decrease in particle size. The particle size continued to decrease with the increase in milling time beyond 45 h, which can be seen in Figure 5. Finally, at 65 h of milling, the formation of equiaxed particles can be observed, which can be attributed to

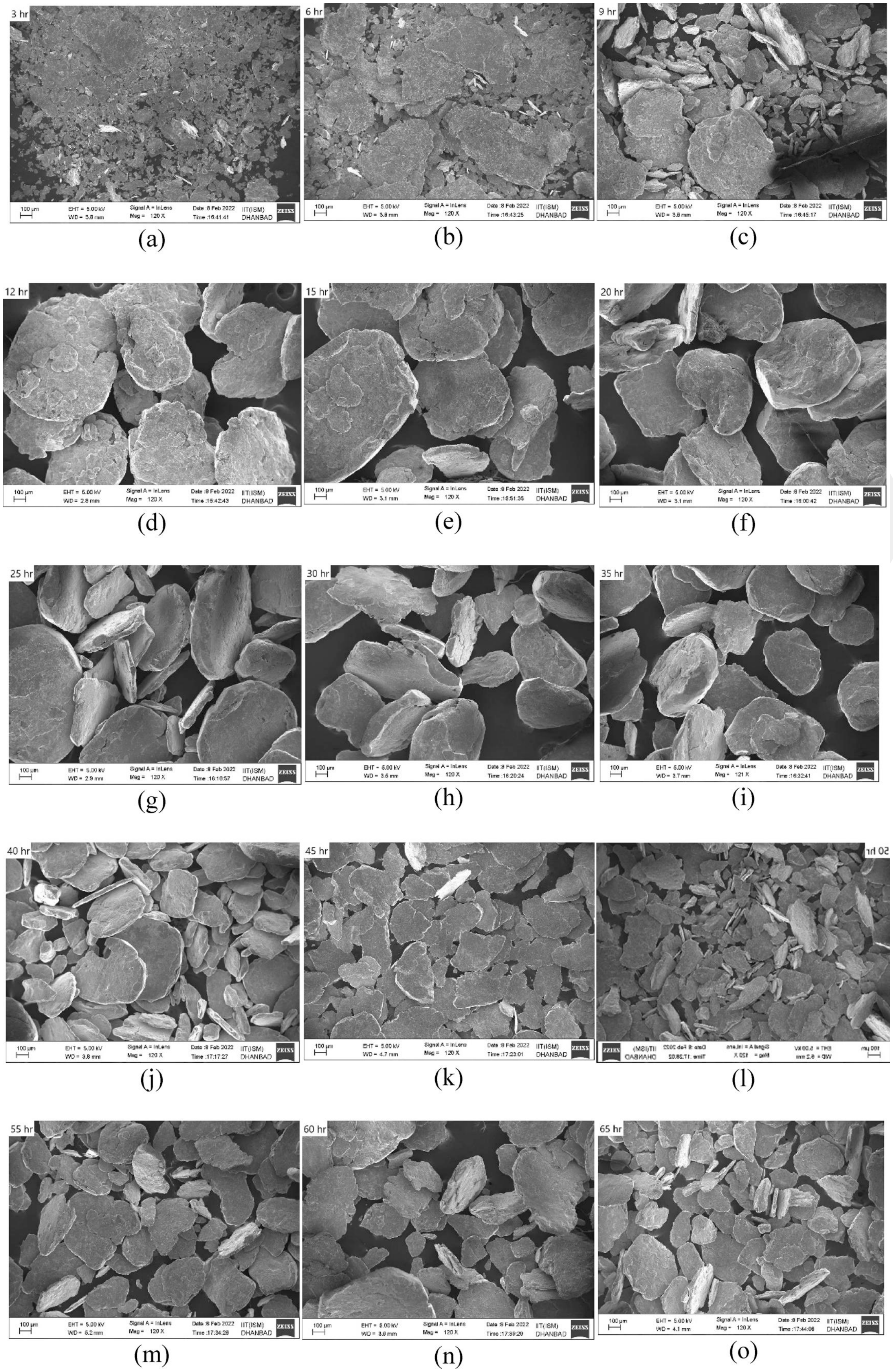

Figure 5. FESEM micrographs depict the Al powder's microstructural evolution with mechanical alloying time. Cold welding corresponds to 12, 15, and 20 h; the equiaxed formation of powder particles can be seen in 65 h.

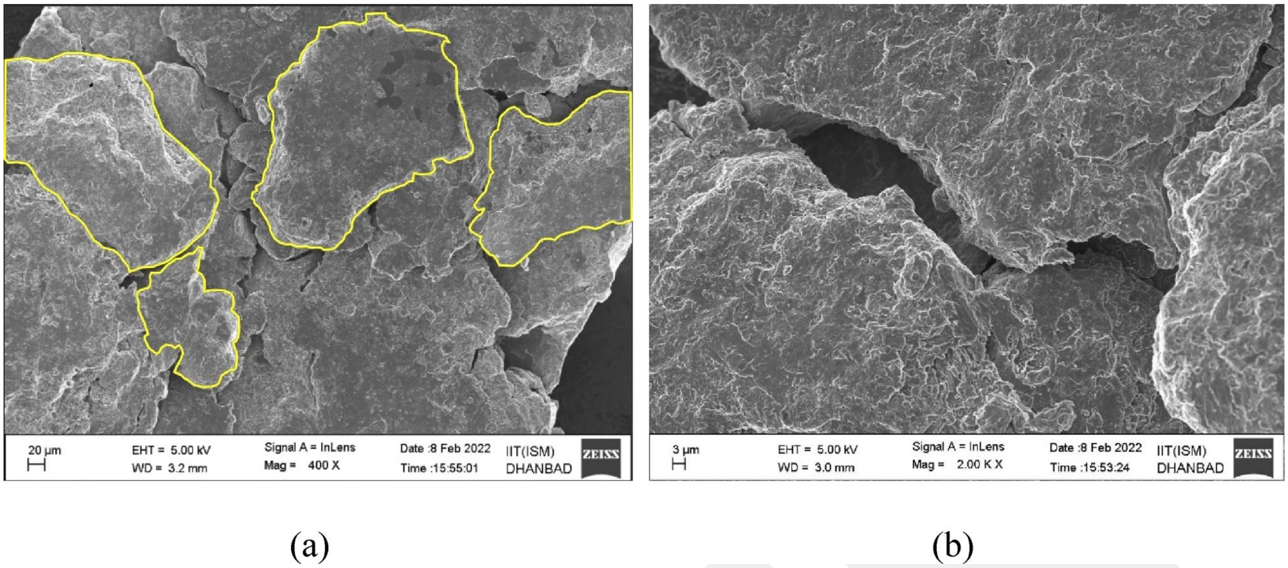

Figure 6. FESEM micrographs show (a) agglomeration of particles, (b) particle fracture boundary of particles during mechanical alloying. Yellow markings represent individual particles resulting in agglomeration.

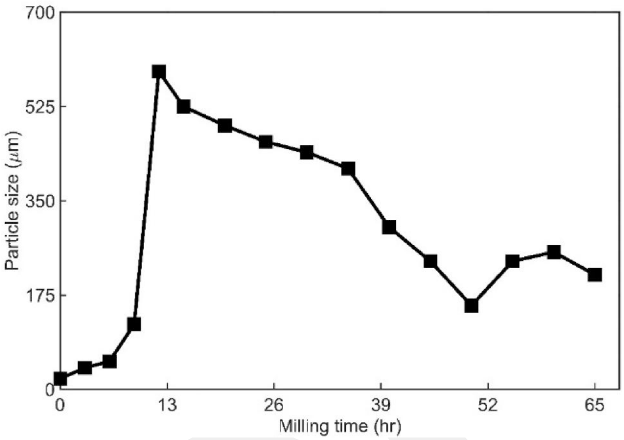

Figure 7. Average particle size variation with milling time. Particle size first increases due to the cold welding of particles, followed by fracturing, which reduces the particle size. The particle size attained the minimum value at the 45th hour.

the fact that a steady state has reached between welding and the fracturing of particles. The particle size measurements of the powder were done with the help of FESEM imaging and are shown in Figure 7.

Figure 8 shows the high-resolution transmission electron microscopy (HRTEM) image and the associated selected area diffraction pattern (SADP) of the Al powder ball milled for 65 h. From Figure 8, the existence of nanostructuring and polycrystallinity in the high-energy ball-milled powder can be readily observed. According to the TEM data, the average grain size of 65 h milled Al powder is estimated to be about 48.23 nm, see Figure 8a, which is marginally different from the size determined about 51.41 nm using the Williamson-Hall relation. It turns out that the average grain size obtained from the Willam-Hall relation is consistent with the grain size given by TEM and could serve as proof of the validity of William-Hall's grain size measurements. Figure 9a and b depicts a detailed view of the microstructure of the grain, depicting lattice fringes, stacking faults, and twin. The formation of the stacking faults and twin morphologies can be attributed to the large deformation induced by the high-energy ball milling. Furthermore, a high resolution TEM image of a single Al nanograin is shown in Figure 9b, which is identified as ∼13 nm in size, and its lattice spacing is 0.233 nm, suggesting it to be Al (111) plane. To ensure any phase changes or contamination in milled samples, an EDS study was conducted in the TEM analysis as shown in Figure 10. The results identify small counts of oxygen peak, possibly due to oxidation during the long milling period. Please also note that the presence of carbon and copper in the EDS spectra is mainly due to the carbon coated copper grids used during the experiment.

2.3. Density measurement

A precise density measurement is carried out to experimentally determine the densities of the fabricated samples, allowing one to assess the presence of any porosity in samples by comparing them with the densities determined theoretically. Here, the bulk CG-Al, and nc-Al samples are weighed in air and distilled water using a high-resolution electronic balance with a resolution of ±0.0001 g, followed by Archimedes's principle to measure the experimental densities. The density of the as-received pure Al was measured to be about 2.70 g/cc. Furthermore, the effect of the ball milling, sintering, and hot extrusion processes on the porosity content of the samples is also explored. The density measurements of non- and ball-milled samples are reported in Table 2. Please note that the porosity content of samples is evaluated using Archimedes' relationship:

$$\text{Porosity}(\%) = \left[1 - \frac{\rho_f}{\rho_s}\right] \times 100 \tag{2}$$

where ρ_f represents the apparent density of the samples and ρ_s denotes the theoretical density of the samples. From Table 2, it turns out that ball milling and hot extrusion significantly decrease the porosity and consequently increase

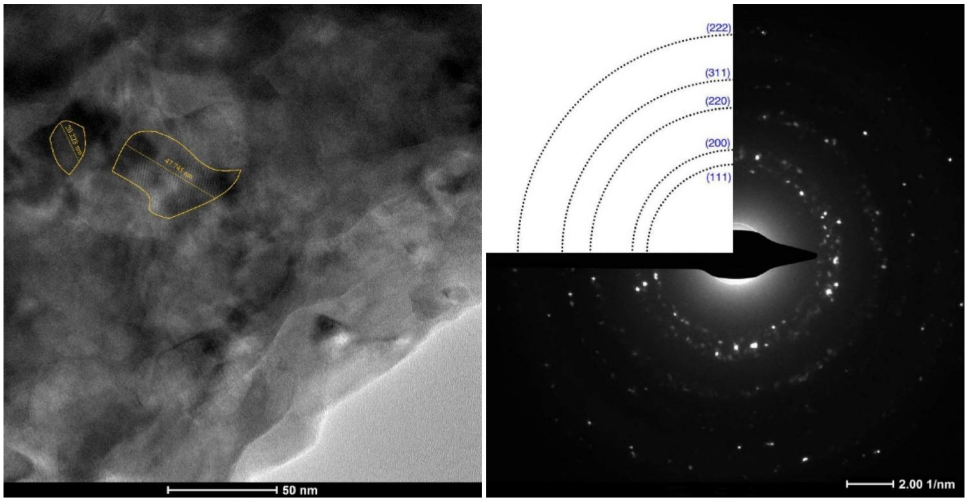

(a) (b)

Figure 8. (a) A HRTEM micrograph of the Al powder milled for 65 h. Yellow lines show two nanograins measuring 20.228 nm and 47.745 nm, (b) corresponding SADP pattern indicating polycrystalline texture; inset indexed radial averaged intensity distribution. Interplanar spacing can be determined by measuring the distance of these rings from the origin.

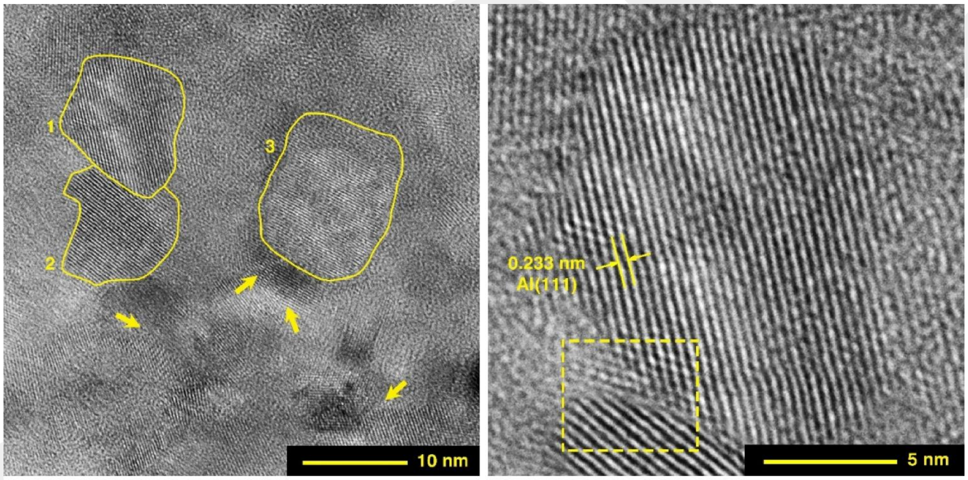

(a) (b)

Figure 9. An HRTEM image showing (a) the crystallographic lattice planes in the nanograins marked with 1, 2, 3; the yellow arrows indicate the stacking faults, (b) enlarged HRTEM of the nanograin 1; a three-fold twin morphology is shown within the yellow rectangle.

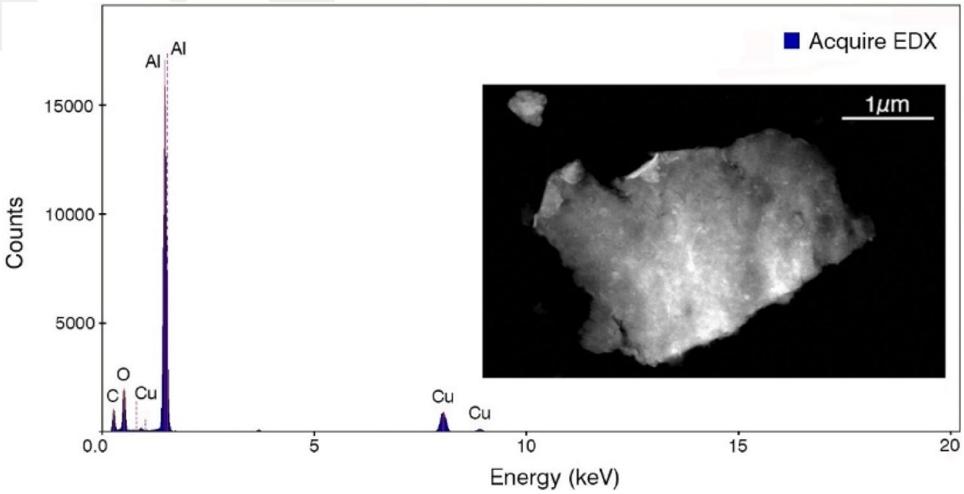

Figure 10. EDS elemental maps of the milled aluminum powders after 65 h of high-energy ball milling processing.

Table 2. Density and porosity measurements of non- and ball-milled pure Al samples undergone sintering and extrusion process.

	Sintered at 550 °C		Extruded at 550 °C	
Materials	ρ [g/cc]	Porosity [%]	ρ [g/cc]	Porosity [%]
Pure Al (unmilled)	2.62 ± 0.0010	2.96 ± 0.006	2.65 ± 0.006	1.85 ± 0.004
Pure Al (milled)	2.64 ± 0.0011	2.22 ± 0.004	2.68 ± 0.006	0.74 ± 0.005

the density of the samples; however, sintering has a moderate impact on them. The ball milling of powders breaks up particle agglomerates, which, in turn, accelerates the diffusion process in sintering, thereby enhancing the density of the samples.

Furthermore, ball milling increases the density of bulk sintered pure Al and bulk extruded pure Al from about 2.62 to 2.64 g/cc and 2.65 to 2.68 g/cc, respectively, and consequently reduces the porosity from about 2.96 to 2.22% and 1.85 to 0.74%, respectively. However, the effect of hot extrusion is more pronounced in obtaining near dense samples. This can be ascribed to applying high pressure at higher temperatures during the extrusion process, which reduce the bubble nucleation and consequently enhance the material density. Extrusion leads to a significant enhancement in density (from about 2.62 to 2.65 g/cc and 2.64 to 2.68 g/cc) and the corresponding reduction in porosity (from about 2.96 to 1.85% and 2.22 to 0.74%) in the extruded samples. Further, it is important to iterate that powder metallurgy products usually exhibit an inevitable amount of porosity [29]. However, here, the porosity content in the synthesized final product is less than 1%, which shows that the proposed synthesizing process can successfully fabricate the samples near to theoretical density.

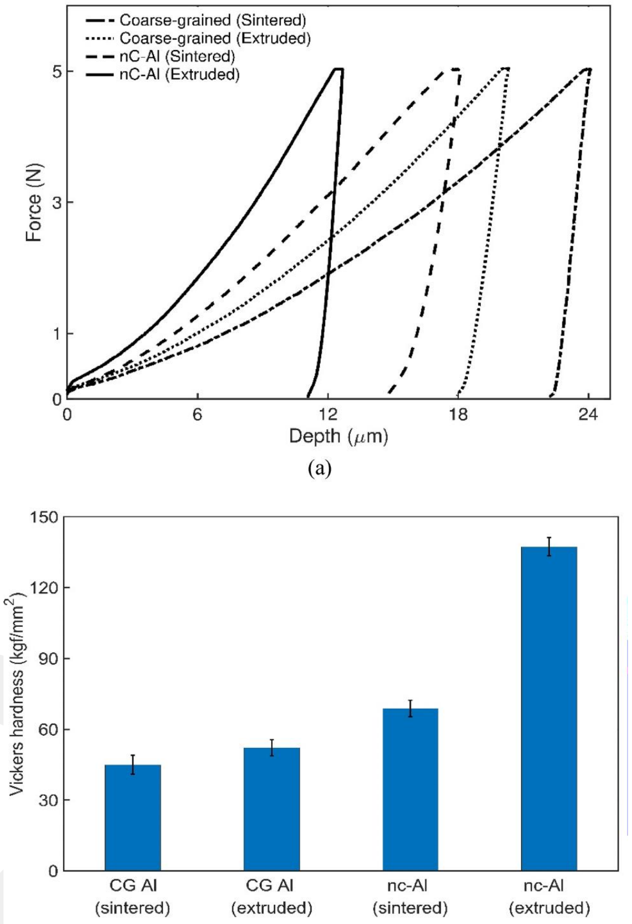

(a)

(b)

Figure 11. (a) Microindentation loading/unloading curves obtained from micro-indentation test, and (b) Vickers hardness measurements for CG-Al and nc-Al under different environments. The microhardness of extruded nc-Al was significantly higher than that of CG-Al. The test was conducted at a loading rate of 5 N/min.

2.4. Microhardness measurement

Here, the hardness of samples, as one of the most crucial material's properties, is evaluated using microhardness tests which enable one to assess a material's properties, such as strength, ductility, and wear resistance, and also helps to determine the suitability of nc-Al for various applications. The test was conducted on the polished samples under an indentation load and dwell time of 5 N and 30 s, respectively, while retaining a high loading rate of 1 N/min during the test to avoid creep in the samples. Figure 11 illustrates loading-unloading results along with the corresponding hardness values for extruded and sintered CG-Al and nc-Al samples obtained from the micro-indentation experiment. From Figure 11a and b, it can be readily seen that the response of the nc-Al sample is steeper than that of CG-Al as an implication of the higher hardness and the modulus value. It turns out that extruded nc-Al exhibit a 160% increase in hardness values (from about 52.2 to 137.3 kgf/mm^2) compared to extruded CG-Al. Therefore, high-energy ball milling significantly reduces the crystal size at the nanoscale and, thus, improves the strength of pure Al following the Hall-Petch relationship [57]. Increasing hardness is mainly due to heavy deformation and grain size reduction by longer milling duration, resulting in the strain hardening of the ductile aluminum alloy powders. It can also be attributed to the accumulation of fine grains on or at grain boundaries, which prevent crack propagation and dislocation movement and thereby increase the microhardness of the material [6]. Moreover, extrusion also plays a significant role in grain refinement, enhancing the material's hardness. However, the effect of extrusion in improving the hardness is more significant in nc-Al than CG-Al. About a 100% increase in hardness can be seen in the extruded nc-Al samples, whereas a 16% rise can be seen in the case of CG-Al samples. This is likely due to the elimination of pores and microvoids in the sintered samples and the formation of a more refined and compact microstructure during extrusion

The hardness measurement is further proceeded by studying the rate sensitivity of nc-Al, an extensive set of micro-indentation tests are conducted at different loading rates of 1.0345 mN/s, 10.345 mN/s, and 103.45 mN/s, respectively. The samples were ground and polished before the indentation tests to ensure they had a deformation-free surface. Here, the strain rate sensitivity, m, is measured using the following expression:

$$m = \frac{\partial \ln(\mathrm{H})}{\partial \ln(\dot{\varepsilon})} \cong \frac{\partial \ln(H_2/H_1)}{\partial \ln(\dot{\varepsilon}_2/\dot{\varepsilon}_1)} \tag{3}$$

where, H and ε represent hardness and strain rate. Using (3), the value of m is determined to be 0.035, representing an eight-fold increase compared to its coarse-grained counterpart. This result is in line with the results of Figure 12a, where the force-depth curve exhibited a considerable loading rate sensitivity. From Figure 12b, it can be seen that the samples tested at the loading rate of 103.45 mN/s exhibits a Vickers hardness of about 179.7 kgf/mm^2, while at the rate of 1.0345 mN/s shows a hardness of about 120.6 kgf/mm^2 which is an implication for the inherent strain rate sensitivity of nc-Al. For the sake of comparison, Table 3 outlines the strain rate sensitivity index for the present samples along with various nanostructured Al materials reported in the literature.

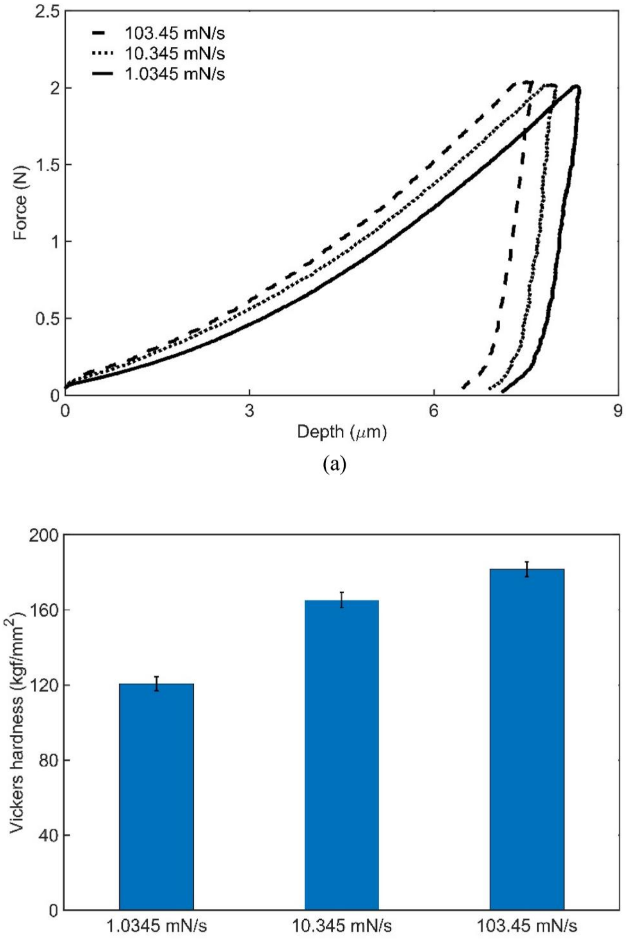

(a)

(b)

Figure 12. (a) Microindentation test result for nc-Al at different loading rates of 103.45 mN/s, 10.345 mN/s, 1.0345 mN/s, and (b) Vickers hardness data for various loading rates. It can be seen that nc-Al displays a strain rate-dependent behavior.

Table 3. Comparison of strain rate sensitivity measurement data for various nanostructured Al and its alloys.

Al alloy	Treatment	Grain size (μm)	Strain rate sensitivity factor, m	Reference
nc-Al*	PM	0.051 ± 0.004	0.035	Present study
nc-Al	PM	0.042 ± 0.004	0.024 – 0.054	[58]
AA6082	ECAP	0.2 – 0.4	0.03	[18]
AA1050	ARB	0.35 – 0.50	0.042 – 0.069	[21]
UFG* Al	cryoPM	0.1 – 0.2	0.03 – 0.06	[32]
UFG Al	ECAP	0.27 – 0.43	0.014	[16]

*Note: nc = nanocrystalline; UFG = ultra fine grain.

2.5. Tensile, compression testing, and fracture behavior

This section elaborates on the experimental methodology employed to characterize the tensile, compression, and fracture behavior of nc-Al. According to ASTM E8/E8M-13a, the tensile test specimens were prepared using a dog-bone geometry of 4 mm gauge diameter and 20 mm gauge length. Tensile testing was performed using the Hounsfield 50 KN tensile testing machine at three various cross-head speeds of 9.6 mm/min, 0.96 mm/min, and 0.096 mm/min, implying various strain rates 0.01 s^{-1}, 0.001 s^{-1} and 0.0001s^{-1} respectively. It is also interesting to identify the degree of tension-compression asymmetry by conducting a compression test. Furthermore, by having no propensity for necking and strain localization, the compression test allows one to characterize the stress-strain response of nc-Al materials at finite strains and deformations. In doing so, following ASTM E9-89a, simple compression tests areperfumed on initially-cylindrical samples with initial diameter and height of 8 mm and 8 mm, respectively at a cross-head speed of 0.096 mm/min, which implies the strain rate of 0.0001s^{-1}. It is also important to note that the results of these uniaxial tests will later be used in the forthcoming sections to calibrate the material parameters introduced by the proposed constitutive theory.

Figure 13a compares the true stress-strain results for the nc-Al obtained from tensile and compression tests at the strain rate of 0.0001s^{-1}. From Figure 13a, it can be seen that the tensile and compressive elastic-plastic flow behavior appears to be very similar, and their strength was estimated at about 315 MPa. Further, it can be observed that there exists a slight asymmetry in tension and compression curves, with the stresses corresponding to strains in the compression curve being slightly higher than the tensile one. However, the differences are insignificant and can be neglected for engineering design and analysis applications. Moreover, both the tensile and compression curve in Figure 13a exhibits three distinct deformation regions; region 1 corresponds to elastic deformation followed by region 2, which indicates strain hardening, but the hardening is restricted to the initial phase (plastic strain $< 2\%$). Region 2 is followed by region 3, which shows softening and eventual fracturing of the samples (for tension). Next, a comprehensive set of tensile experiments were conducted to elucidate the effect of strain rate sensitivity on the material strength and ductility cf., Figure 13b. It turns out that with the increase in the strain rate, there exists a considerable increase in the flow stress value and reduction in ductility, indicating that strain rate strongly influences deformation behavior. Tensile strength of about 371 MPa was observed at a strain rateof 0.01 s^{-1}, which corresponds to a uniform ductility of about 16.5%; meanwhile, the ductility, measured by the strain to failure, is enhanced to about 28.5% by compensating the tensile strength to about 315 MPa at a strain rate of 0.0001s^{-1}. Therefore it can be concluded that the material displays a greater elongation, however, at the cost of some strength and vice versa. The tensile ductility in this work is higher than that reported by Ahmed et al. [59] for nc-Al samples (grain size *29 nm), which showed a total ductility of about 11.5%, and also greater than that of nc Al produced

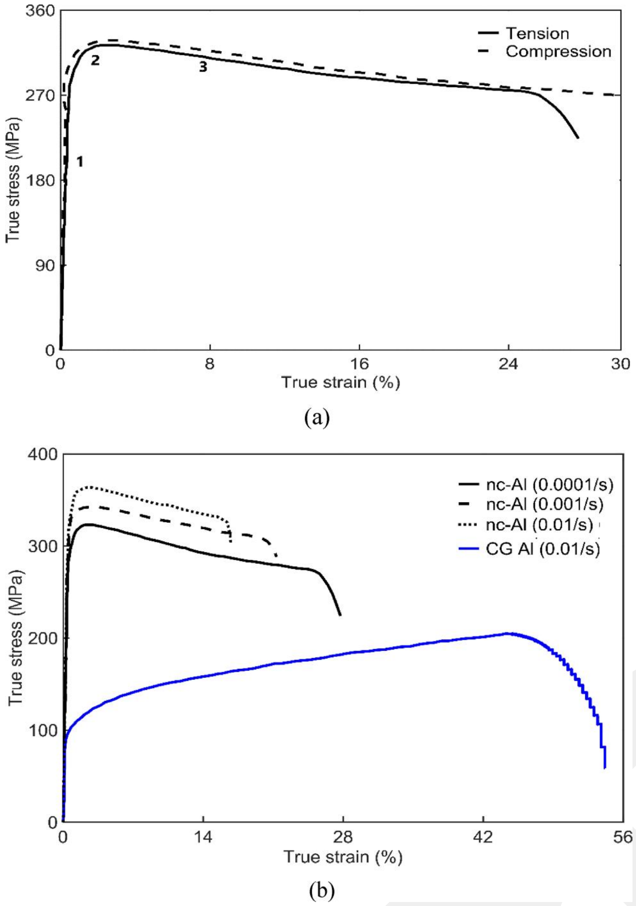

(a)

(b)

Figure 13. (a) Tensile and compression true stress-strain curves for nc-Al at a strain rate of $0.0001\,s^{-1}$. Indexes 1, 2, and 3 represent three deformation regions: elastic, strain hardening, softening & eventual fracturing. (b) The black lines represent tensile true stress-strain curves for nc-Al at different strain rates of $0.0001\,s^{-1}$, $0.001\,s^{-1}$, and $0.01\,s^{-1}$. The blue line represents tensile true stress-strain curves for CG-Al at strain rates of $0.01\,s^{-1}$.

by friction extrusion, which failed at plastic deformation of about 16.5% in tension [3] (For more information, see Table 4). The high tensile ductility ensured the integrity of the in-situ consolidated nanostructure and didn't exhibit any signs of tensile instability or processing artifacts commonly found in nanocrystalline materials. Dislocation slip processes and activated twins have likely caused the high tensile ductility during deformation. In addition, the nc Al developed demonstrated an about 163% increase in tensile strength over its coarse grained counterpart.

To broaden our understanding corresponding to the fracture of the tensile samples performed at different strain rates, a fractography analysis of the samples is conducted, as shown in Figure 14. As shown in Figure 14, each fractured surface is adorned with multiple micro-voids and dimples, indicative of a ductile fracture. Here, the nc-Al sample subjected to a strain rate of $0.0001s^{-1}$ shows large and deep dimples compared with the samples subjected to a higher strain rate of $0.01\,s^{-1}$. In fact, as an index for the material ductility, these large and deep dimples in the fracture surface for the specimen loaded at the rate of $0.0001s^{-1}$ provide compelling evidence of ductility that help samples to undergo the large strain of about 28.5% for, as compared to the sample loaded at the rate of $0.01\,s^{-1}$ which experience at most the strain of 16.75%.

3. Constitutive modeling

This section introduces a continuum-level constitutive modeling approach and its finite element implementation that can be employed to design and analyze structural components made of bulk nanocrystalline aluminum. Furthermore, an ad-hoc curve fitting procedure is proposed to calibrate the newly-introduced constitutive material parameters effectively. Finally, the predictive capabilities of the theory are experimentally verified for tension, compression, and Vickers Microindentation experiments at various loading rates.

3.1. Summary of the constitutive theory

Recently, Wei, and Anand [52] have proposed a constitutive theory for designing and analyzing structures made of powder-processed nanocrystalline metals. The theory has been well-validated for Mg and Cu-based nanocrystalline metals by comparing various numerical results with experimental data. Following the work by Wei, and Anand [52], a continuum-scale constitutive modeling approach is proposed as a mathematical framework to describe the nc-Al mechanical response in arbitrary contexts. The core idea of the modeling is to exploit the similarities between the deformation mechanisms of consolidated-powder metals and the cohesive granular materials in the macroscopic scale to develop an isotropic rate-dependent elastic-plastic theory for powder-proceed metals [52]. In the present theory, the pressure dependency of the powder-processed metals is accounted for by a plastically dilatant and non-normal flow rule formulated in a hyperelastic-based finite deformation setting.

Notations. The following standard notation of modern continuum mechanics is used throughout the text[1]:

ψ	Free energy density, measured per unit relaxed volume
$\mathbf{F} = \partial \mathrm{x}/\partial \mathbf{X},\ J = \det\mathbf{F} > 0$	Deformation gradient
$\mathbf{F} = \mathbf{F}^e\mathbf{F}^p$	Multiplicative decomposition
$\mathbf{F}^p,\ J^p = \det\mathbf{F}^p > 0$	Plastic distortion
$\eta = \ln(J^p)$	Plastic volumetric strain
$\mathbf{F}^e,\ J^e = \det\mathbf{F}^e > 0$	Elastic distortion
$\mathbf{F}^e = \mathbf{R}^e\mathbf{U}^e$	Polar decomposition of $\mathbf{F}^e$
$\lambda^e_\alpha, \mathbf{r}_\alpha$	Eigenvalues and eigenvectors of $\mathbf{U}^e$
$\mathbf{U}^e = \sum_{\alpha=1}^{3} \lambda^e_\alpha \mathbf{r}_\alpha \otimes \mathbf{r}_\alpha$	Spectral decomposition of $\mathbf{U}^e$
$\mathbf{E}^e = \sum_{\alpha=1}^{3} (\ln\lambda^e_\alpha)\mathbf{r}_\alpha \otimes \mathbf{r}_\alpha$	Logarithmic elastic strain
$\mathbf{T}, \mathbf{T} = \mathbf{T}^\top$	Cauchy stress
$\mathbf{T}^e = J^e\mathbf{R}^{e\top}\mathbf{T}\mathbf{R}^e$	Stress conjugate to $\mathbf{E}^e$

---

[1] The notation $\mathbf{A}$ stands for a second-order tensor with $A^\top$ as the transpose of $\mathbf{A}$. The quantities, $\mathrm{tr}\mathbf{A}$, $\mathrm{dev}\,\mathbf{A} = \mathbf{A} - (1/3)(\mathrm{tr}\,\mathbf{A})\mathbf{I}$ and $|A| = \sqrt{A : A}$ denote the trace of tensor $\mathbf{A}$, the deviatoric part of tensor $\mathbf{A}$ and the magnitude of tensor $\mathbf{A}$, respectively, such that $\mathbf{A} : \mathbf{A} = \mathrm{tr}(\mathbf{B}^\top\mathbf{A})$ denote the scalar product of two second-order tensors $\mathbf{A}$ and $\mathbf{B}$. The vectors $\mathbf{X}$ and x represent the *reference* position and *current* position, respectively.

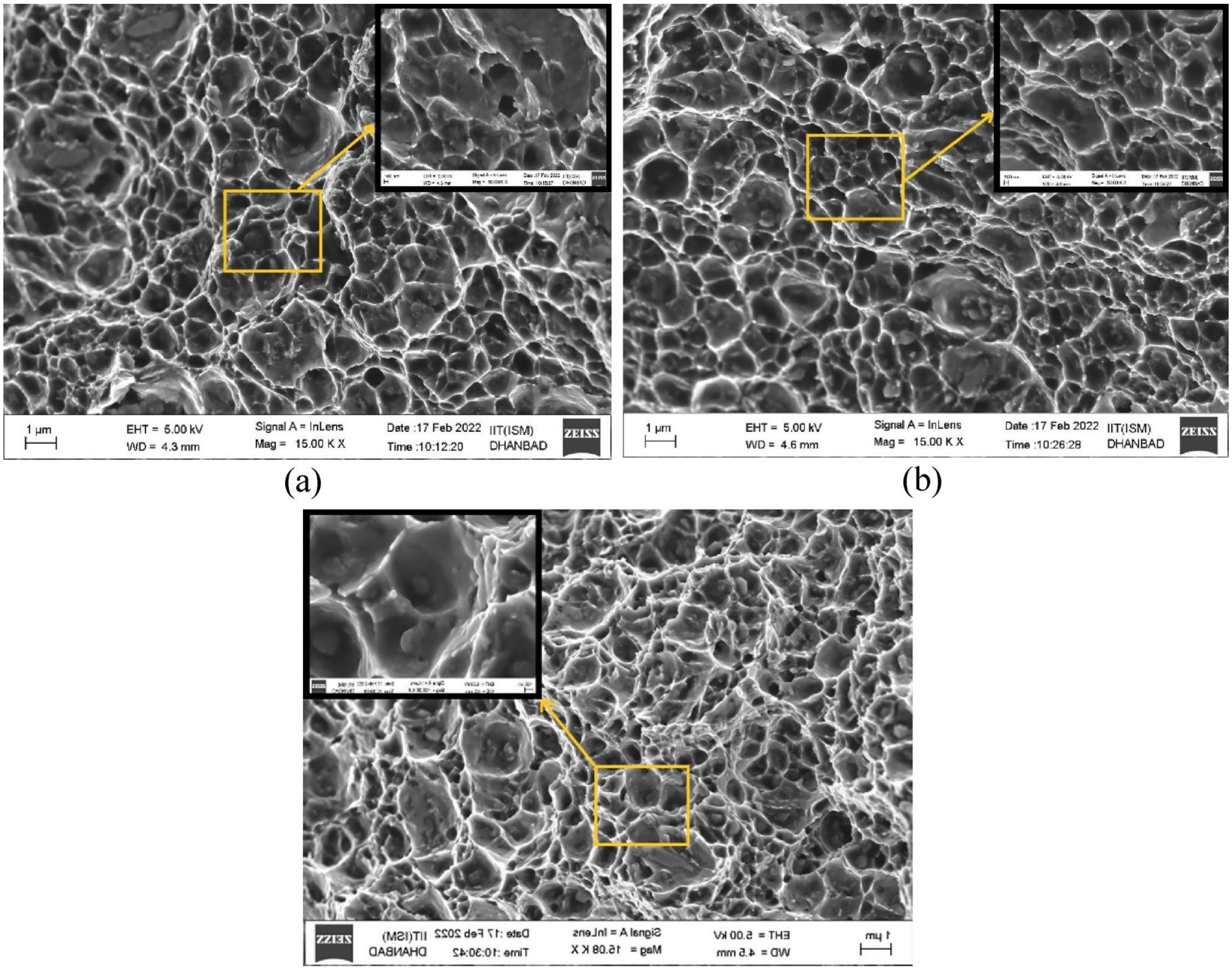

(a) (b)

(c)

Figure 14. FESEM fractography showing the fracture surfaces of nc-Al subjected to a strain rate of (a) 0.0001 s^{-1}, (b) 0.001 s^{-1}, and (c) 0.01 s^{-1}. The dimple fracture mechanism is the dominant fracture mode observed in all the cases. Insets represent higher-magnification images corresponding to the respective yellow rectangle region.

Table 4. Comparative data for the properties for various nanostructured Al and its alloys.

Material	Grain size (μm)	0.2% Offset YS (MPa)	UTS (MPa)	Fracture strain (%)	Refere-nce
nc-Al*	0.051 ± 0.004	328 ± 4	371 ± 5	16.75 ± 1.1	Present study
ns-Al	0.084 ± 0.007	255.1 ± 10	300.2 ± 14.4	8 ± 1.3	[60]
ns-AA2124	–	88 ± 10	350 ± 12	11.5 ± 1	[43]
ns-CNT/Al(HSBM)	0.217	384 ± 7	408 ± 1	4 ± 0.3	[44]
ns-CNT/Al(SSBM)	0.308	326 ± 21	376 ± 3	12.4 ± 1.3	[44]
ns-Al	0.5	237 ± 2	300 ± 2	11.4 ± 0.6	[45]
ns-Al2024	–	698	712	4.2	[61]
nc-Al	0.029	375	410	11.5	[59]
nc-Al	–	125	147	18	[62]

*Note: ns: nanostructured; HSBM: high speed ball milling; SSBM: shift speed ball milling; YS: yield strength; UTS: ultimate tensile strength.

- *Free energy density*: We take the free energy density, ψ as

$$\psi = \hat{\psi}(\mathbf{E}^e) = G|\mathrm{dev}\mathbf{E}^e|^2 + K(\mathrm{tr}\mathbf{E}^e)^2 \tag{4}$$

where G and K are the elastic shear and bulk moduli.

- *Stress-strain relation:* The stress-strain relation is given as

$$\mathbf{T}^e = \frac{\partial\psi}{\partial\mathbf{E}^e} = 2G\left(\mathbf{E}_0^e\right) + K\left(\mathrm{tr}\mathbf{E}^e\right)\mathbf{I} \tag{5}$$

- *Dilation based non-normal flow rule:* Assuming the plastic spin rate $\mathbf{W}^p = 0$, the evolution of the plastic deformation gradient, $\mathbf{F}^p$ is taken to be

$$\dot{\mathbf{F}}^p = \mathbf{D}^p\mathbf{F}^p \ \text{with} \ \mathbf{F}^p(\mathbf{X}, 0) = \mathbf{I} \tag{6}$$

where the plastic stretch rate, $\mathbf{D}^p$ is given by

$$\mathbf{D}^p = \mathbf{D}_s^p + \mathbf{D}_c^p \tag{7}$$

and it is induced by two microstructure-based mechanisms, namely the shear dominated micromechanism, $\mathbf{D}_s^p$, and the cavitation-induced micromechanism, $\mathbf{D}_c^p$.

The shear-dominated contribution, $\mathbf{D}_s^p$ is proposed in the form of

$$\mathbf{D}_s^{\mathrm{p}} = \mathrm{dev}\ \mathbf{D}_s^{\mathrm{p}} + \frac{1}{3}\mathrm{tr}\ \mathbf{D}_s^{\mathrm{p}}\mathbf{I} \tag{8}$$

such that

$$\mathrm{dev}\ \mathbf{D}_s^{\mathrm{p}} = d^p\mathbf{N}^{\mathrm{p}} \text{ and } \mathrm{tr}\ \mathbf{D}_s^{\mathrm{p}} = \beta \mathrm{d}^{\mathrm{p}}. \tag{9}$$

Note that the first term on the right-hand side of (8) represents the purely isochoric portion of $\mathbf{D}_s^{\mathrm{p}}$, and the second term on the right-hand side of (8) represents the purely volumetric (that is, the shear-induced dilatancy) portion of $\mathbf{D}_s^{\mathrm{p}}$.

The quantities $d^p = \sqrt{2}\left|dev\ \mathbf{D}_s^p\right| \geq 0$ and $\mathbf{N}^{\mathrm{p}} = (1/2)\ \mathrm{dev}\mathbf{T}^{\mathrm{e}}/\overline{\tau}$ stand for the equivalent plastic shear strain rate, and the direction of deviatoric plastic flow, respectively. Using a power-law constitutive function, the equivalent plastic shear strain rate d^p is defined as

$$d^p = d_0\left[\frac{\overline{\tau}}{c + \mu\overline{p}}\right]^{1/m} \tag{10}$$

with $\overline{\tau} = \sqrt{1/2}\ |\mathrm{dev}\mathbf{T}^{\mathrm{e}}|$ representing the equivalent shear stress. The quantities $\overline{p} = -(1/3)\mathrm{tr}\ \mathbf{T}^e$, $c > 0$ and $\mu \geq 0$ denote the mean-normal pressure, internal cohesion variable, and friction internal variable, respectively. Further, $d_0 > 0$ and $m > 0$ are the reference plastic shear strain rate and the strain-rate sensitivity parameter, respectively. Note that the quantity $\mu\overline{p}$ controls the pressure sensitivity of plastic flow.

The shear-induced plastic dilatancy parameter, β can be related to the plastic volumetric strain through $\eta = \ln(J^p)$ and it can be defined by

$$\beta = g_0\left[1 - \frac{\eta}{\eta^*}\right] \tag{11}$$

where $g_0 > 0$ and $\eta^* > 0$ are the experimentally-determined material parameters. It is important to remark that the present formulation uses a non-associated flow rule due to $\mu \neq \beta$ for avoiding excessive plastic volumetric dilation leading to spurious results.

The cavitation mechanism, $\mathbf{D}_c^p$ is determined by the following constitutive relation,

$$\mathbf{D}_c^p = \sum\nolimits_{\mathrm{i}=1}^{3} d_c^{(i)}(\hat{\mathbf{e}}_{\mathrm{i}} \otimes \hat{\mathbf{e}}_{\mathrm{i}}) \tag{12}$$

with

$$d_c^{(i)} = \begin{cases} d_0\left[\frac{\sigma_i - \sigma_{th}}{\sigma_{cr}}\right]^{1/m} & \text{if } \sigma_i > \sigma_{th} \\ 0 & \text{otherwise} \end{cases} \tag{13}$$

where the quantity $\sigma_{cr} = c_1 + c_2\overline{p}$ is linearly correlated to $(-\overline{p})$ through the material parameters c_1 and c_2. The eigenvalues of the stress tensor, σ_i can be determined by recasting the stress tensor $\mathbf{T}^{\mathrm{e}}$ into its spectral representation form as follows:

$$\mathbf{T}^e = \sum\nolimits_{i=1}^{3} \sigma_i(\hat{\mathbf{e}}_{\mathrm{i}} \otimes \hat{\mathbf{e}}_{\mathrm{i}}) \text{ such that } \sigma_1 \geq \sigma_2 \geq \sigma_3 \tag{14}$$

Please note that the parameters d_0 and m used in (13) are taken to be the same as that in (10), for the sake of simplicity.

- *Kinetic rate-formed equations of internal variables:* Due to the scarcity of available physics-based experimental evidence for the evolution of the internal friction μ in cohesive powder-consolidated nanocrystalline materials, it is therefore assumed to be

$$\mu \ \equiv \mathrm{Constant} > 0 \tag{15}$$

Using (7), (8) and (12) into $\eta = \ln(J^p)$ and taking the time derivative results in

$$\dot{\eta} = \mathrm{tr}\mathbf{D}^{\mathrm{p}} = g_0\left[1 - \frac{\eta}{\eta^*}\right]d^p + \sum\nolimits_{\mathrm{i}=1}^{3} d_c^{(i)} \text{ with } \eta(0) = 0 \tag{16}$$

The evolution equation for the cohesion parameter, c can be written using a phenomenological expression as follows

$$\dot{c} = \left[h_0\left|1 - \frac{c}{c^*}\right|^a \mathrm{sign}\left(1 - \frac{c}{c^*}\right)\right]d^p - h_c\sum\nolimits_{i=1}^{3} d_c^{(i)} \tag{17}$$

with

$$c^* = \overline{c}\left[\frac{d^p}{d_0}\right]^n + b(\eta^* - \eta) \quad \text{and} \quad c(0) = c_0 \tag{18}$$

In summary, the present constitutive equations can be fully calibrated by identifying the following constitutive parameters set

$$\{G, K, d_0, h_0, n, c_1, \sigma_{th}, m, a, b, c_2, h_c, \mu, c_0, \eta^*, \overline{c}, g_0\} \tag{19}$$

Finally, the proposed model is integrated into Abaqus/Explicit package *via* a user defined material subroutine using an explicit-based numerical time integration scheme. Careful considerations are therefore given for selecting the suitable size of time steps in finite element simulations to avoid possible inaccuracies raised by solution instability. Algorithm 1 presents the details of the explicit-based time integration scheme used to implement the present constitutive equation into the Abaqus/Explicit package. Please note that subscripts t and τ denote the corresponding notation at the current time t and $t + \ \Delta t$, respectively, where $\Delta t > 0$ refers to a small increment in time. Furthermore, it is noteworthy that the Newton-Raphson method is employed to update the internal variables by solving the set of non-linear scalar equations.

3.2. Material parameters calibration procedure

At this point, an ad-hoc curve fitting material calibration procedure proposed by Wei, and Anand [52] is outlined. The fitting process was performed through the C3D8R, 8-node linear brick, reduced integration Abaqus/Explicit element.

The parameters $\{G,\ K\}$ can be determined from the bulk CG-Al with a good estimation. The elastic shear modulus, $G = 26.0$GPa and the elastic bulk modulus, $K = 76.1$GPa, are obtained from Ledbetter, and Reed [63] at room temperature. The referential strain rate, d_0, is set to the lowest in the simple tensile experiment. The parameters $\{c_0 \ and \ \overline{c}\}$ controlling the initial strength and the stabilized flow stress under shearing (i.e. $\eta * \ = \eta$) can be identified by reproducing the tensile response curve obtained from a simple tensile experiment. The parameters $\{b,\ g_0,\ \eta^*\ \}$ can be calibrated by fitting the model to the strain-softening portion of the curve caused by shear-induced dilatancy. As discussed in [52], the quantity $b(\eta - \eta^*)$ is responsible for the difference of the peak stress with the fully-developed flow stress on the stress strain curve, and the parameter g_0 characterizes the initial rate of strain softening.

```
Algorithm 1 Explicit-based numerical time integration algorithm
Data: $\mathbf{F}_t, \mathbf{T}_t, \mathbf{R}^e_t, \mathbf{F}^p_t, \mathbf{F}_\tau, c_t, \eta_t$ (saved as internal variables);
Result: $\mathbf{T}_\tau, \mathbf{F}^p_\tau, c_\tau, \eta_\tau$
Initialization;
Stress pull-back transformation: $\mathbf{T}^e_t \leftarrow (\det \mathbf{F}^e_t)\mathbf{R}^{e\top}_t \mathbf{T}_t \mathbf{R}^e_t$;
Volumetric-deviatoric decomposition: $\operatorname{dev} \mathbf{T}^e_t \leftarrow \mathbf{T}^e_t + \left(\frac{1}{3}\right)(\operatorname{tr} \mathbf{T}^e_t)\mathbf{I}$;
Equivalent shear stress and mean normal pressure: $\bar{\tau}_t \leftarrow \sqrt{\frac{1}{2}}|\operatorname{dev} \mathbf{T}^e_t|$ and $\bar{p}_t \leftarrow -\left(\frac{1}{3}\right)\operatorname{tr} \mathbf{T}^e_t$
Direction of deviatoric plastic flow: $\mathbf{N}^p_t \leftarrow \frac{\left(\frac{1}{2}\right)\operatorname{dev} \mathbf{T}^e_t}{\bar{\tau}_t}$;
Equivalent plastic shear strain rate using (10);
Plastic stretch rate & plastic distortion: $\mathbf{D}^p_t \leftarrow \mathbf{D}^p_s + \mathbf{D}^p_c$ and $\mathbf{F}^p_\tau \leftarrow \left[\mathbf{I} - \Delta t \mathbf{D}^p_t\right]^{-1}\mathbf{F}^p_t$;
Elastic distortion & new elastic Hencky strain: $\mathbf{F}^e_\tau \leftarrow \mathbf{F}_\tau \mathbf{F}^{p-1}_\tau$ and $\mathbf{E}^e_\tau \leftarrow \log(\mathbf{U}^e_\tau)$;
New corotated Kirchhoff stress using (5);
Stress push-forward transformation: $\mathbf{T}_\tau \leftarrow \frac{1}{\det(\mathbf{F}^e_\tau)\mathbf{R}^e_\tau \mathbf{T}^e_\tau \mathbf{R}^{e\top}_\tau}$
while $i < i_{\max}$ do
    ${}^{i}f(c_\tau, \eta_\tau) \leftarrow c_\tau - c_t - \Delta c(c_\tau, \eta_\tau)$;  /* Loop for Newton-Raphson method*/
    ${}^{i}g(c_\tau, \eta_\tau) \leftarrow \eta_\tau - \eta_t - \Delta\eta(c_\tau, \eta_\tau)$;
    $\begin{Bmatrix} {}^{i+1}c_\tau \\ {}^{i+1}\eta_\tau \end{Bmatrix} \leftarrow \begin{Bmatrix} {}^{i}c_\tau \\ {}^{i}\eta_\tau \end{Bmatrix} - \begin{bmatrix} i(\partial f/\partial c_\tau) & i(\partial f/\partial \eta_\tau) \\ i(\partial g/\partial c_\tau) & i(\partial g/\partial \eta_\tau) \end{bmatrix}^{-1} \begin{Bmatrix} {}^{i}f(c_\tau, \eta_\tau) \\ {}^{i}g(c_\tau, \eta_\tau) \end{Bmatrix}$;
    $\epsilon_p \leftarrow |{}^{i+1}c_\tau - {}^{i}c_\tau| / |{}^{i+1}c_\tau|$;
    $\epsilon_\eta \leftarrow |{}^{i+1}\eta_\tau - {}^{i}\eta_\tau| / |{}^{i+1}\eta_\tau|$;
    if $\epsilon_p < \delta \& \epsilon_\eta < \delta$ then
        Break;
    end
end
*Note: $i$ and $i_{max}$ denote the iteration counter and maximum allowable iteration number, respectively; $\epsilon_c$and $\epsilon_\eta$ denote the error corresponding to $c$ and $\eta$ respectively; $\delta = 1e^{-6}$is convergence tolerance.
```

By comparing the flow strength between tension and compression experiment test data and the referential strain rate, the friction coefficient μ can be approximated. The parameters m and n controlling the rate-sensitivity features of the model can be identified from stress-strain curves at different strain rates. Due to the lack of available experimental reports for estimation of σ_{th} and h_c, these parameters are set to zero for the sake of simplicity. Furthermore, the ideal identification method for the cavitation related parameters $\{c_1, \ c_2\}$ is to fit the model with experimental setups such as the notched bar tension test where cavitation effects are significant. However, as a first-cut assumption, we estimate the parameters using the values reported for an Mg-based nanocrystalline [52]. The constitutive parameters identified for the present powder processed Al-based nanocrystalline metal are summarized in Table 5. To ascertain the accuracy and validity of the presented constitutive theory, the following sections are dedicated to comparative studies between the numerical predictions obtained from finite element simulations with the experimental data determined from the testing apparatus established in Section 2.

3.3. Compression and tension experiments

This section employs the constitutive theory suitably calibrated for nc-Al to predict the uniaxial stress-strain response obtained from uniaxial tension and compression tests. Tensile tests were conducted on dog-bone shape samples with a 4 mm gauge diameter and 20 mm gauge length prepared according to ASTM E8/E8M-13a using the Hounsfield 50 KN tensile testing machine. The experimental stress-strain data were obtained for three different strain rates of $0.0001\mathrm{s}^{-1}$, $0.001\,\mathrm{s}^{-1}$, and $0.01\,\mathrm{s}^{-1}$ at room temperature. Following ASTM E9-89a, simple compression tests were performed on initially-cylindrical samples with initial diameter and height of 8 mm and 8 mm, respectively, at a cross-head speed of 0.096 mm/min, which implies the strain rate of $0.0001\mathrm{s}^{-1}$. The geometrical information of the tensile and compression test specimens are illustrated in Figure 15a and b, respectively. It is important to note that the compression cylindrical specimens were very well polished at both ends to ensure the samples' ends' flatness. In addition, Teflon sheets were considered between the sample and the test platens to significantly alleviate the side effects of friction at interfaces, which can lead to finite homogeneous deformation. The finite element simulations were conducted using a single Abaqus reduced-integration continuum three-dimensional brick (C3D8R) element, see Figure 16. The C3D8R element with three displacement degrees of freedom at corner nodes is a general-purpose element extensively used for structural analysis. The square faces AA'D'D, AA'B'B and ABCD are restricted from motion along axis-1, 2, and 3, respectively. The remaining lateral faces, whose normals coincide with axis-1 and 2, are free to reflect traction-free conditions. The face A'B'C'D' is subjected to positive or negative displacement along its normal to simulate tensile or compression tests, respectively.

Figure 17a compares the true stress-strain prediction obtained from finite element simulation with the experimental stress-strain data obtained from the tensile test carried out at different strain rates of $0.0001\mathrm{s}^{-1}$, $0.001\,\mathrm{s}^{-1}$ and $0.01\,\mathrm{s}^{-1}$. From Figure 17, it turns out that the proposed model and its computational implementations can rigorously address the rate-sensitivity features of the material such that the flow stress increases with increasing strain rate. Furthermore, it can be readily seen that the

Table 5. Summary of constitutive parameters calibrated for the present powder-processed Al-based nanocrystalline metal.

G	26.0 [GPa]	K	76.1 [GPa]	d_0	0.0001 [s^{-1}]	h_0	24.5 [GPa]
n	0.04	c_1	2.5 [GPa]	σ_{th}	0.0 [GPa]	m	0.035
a	1.11	b	19 [GPa]	c_2	11	h_c	0.0 [GPa]
μ	0.03	c_0	140 [MPa]	η^*	0.002 [GPa]	$\bar{c}$	120 [MPa]
g_0	0.006 [GPa]						

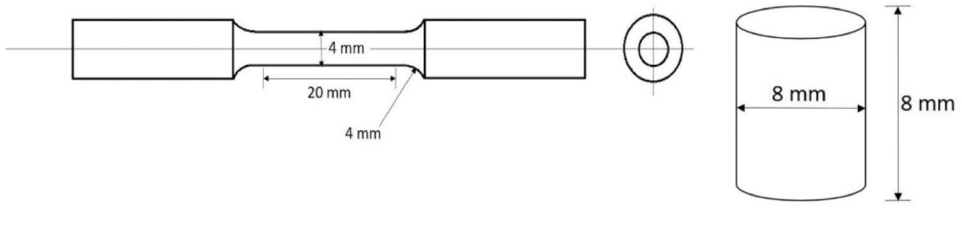

(a) (b)

Figure 15. An Abaqus reduced-integration continuum three-dimensional brick (C3D8R) element used for compression and tension test simulations.

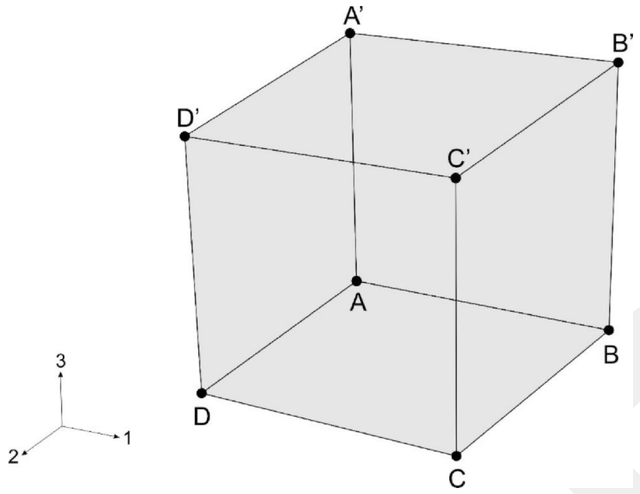

Figure 16. Result of experimental and finite element analysis. (a) True stress-strain curve for nc-Al in tension at strain rates of 0.0001 s s^{-1}, 0.001 s^{-1}, and 0.01 s^{-1}. (b) True stress-strain curve for nc-Al in tension and compression at the strain rate of 0.0001 s^{-1}. The constitutive model successfully reproduces the tension and compression data in good accord.

finite element simulation results are in good agreement with the test data obtained from the experimental apparatus proposed in Section 2. For further verification of the present constitutive model, Figure 17b compares numerical results with the simple compression test data conducted on the nc-Al samples under a strain rate of $0.0001 s^{-1}$. As seen from Figure 17b, the finite element simulation results are consistent with physical experimental data. Therefore, it turns out that the proposed model and its computational implementation can reasonably predict the simple compression test.

3.4. Vickers microindentation experiment

In this section, we further validate the present constitutive modeling approach and its computation implementations with respect to independent Vickers microindentation experiments. Independent validation with respect to such boundary value problems is useful for showing the capability of the model for predicting deformation behavior under multi-axial conditions and localized deformations [64–68]. The Vickers microindentation experiment conducted on nc-Al material can be numerically simulated using the numerical test setup shown in Figure 18a. The symmetrical features of the test setup with respect to the xz and yz planes imply a geometric simplification allowing a significant reduction in computational burdens. The geometrical measurement used in this setup is specified in View A, shown in Figure 18a. In doing so, one-quarter of the geometry is modeled by imposing appropriate symmetric boundary conditions on xz and yz symmetry planes. The nc-Al sample has been spatially discretized using a general purpose linear brick element with reduced integration (C3D8R element). The initially undeformed mesh assigned to the nc-Al sample at the microindenter tip region is shown in 'Detail **B'**' in Figure 18a. It is worth noting that a comprehensive mesh convergence study was carried out to find the solution that required the least amount of computing while providing the highest accuracy.

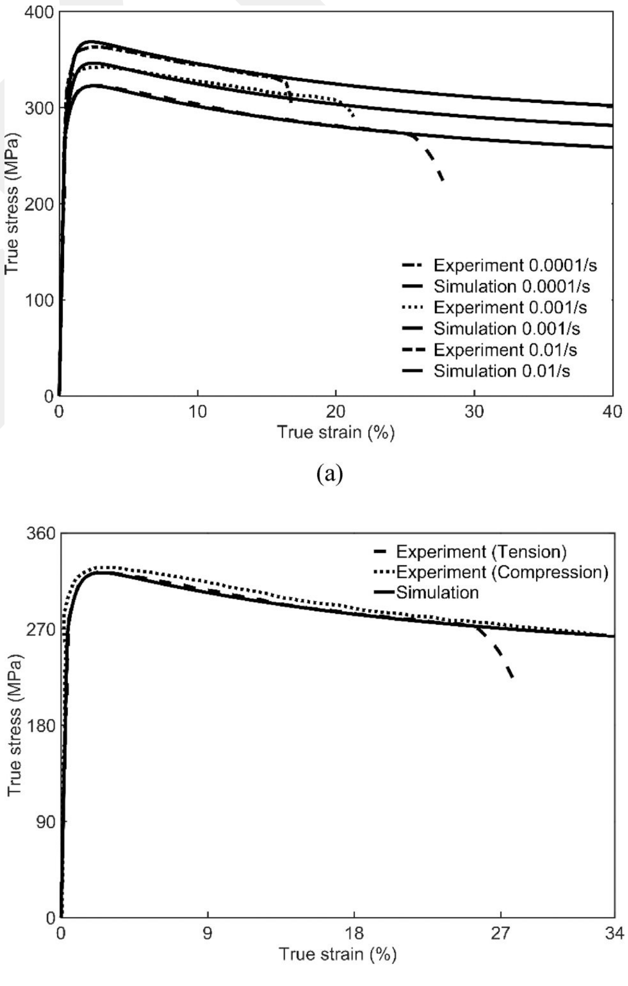

(a)

(b)

Figure 17. Geometries of the (a) tensile specimen and (b) compression specimen used in tensile and compression tests.

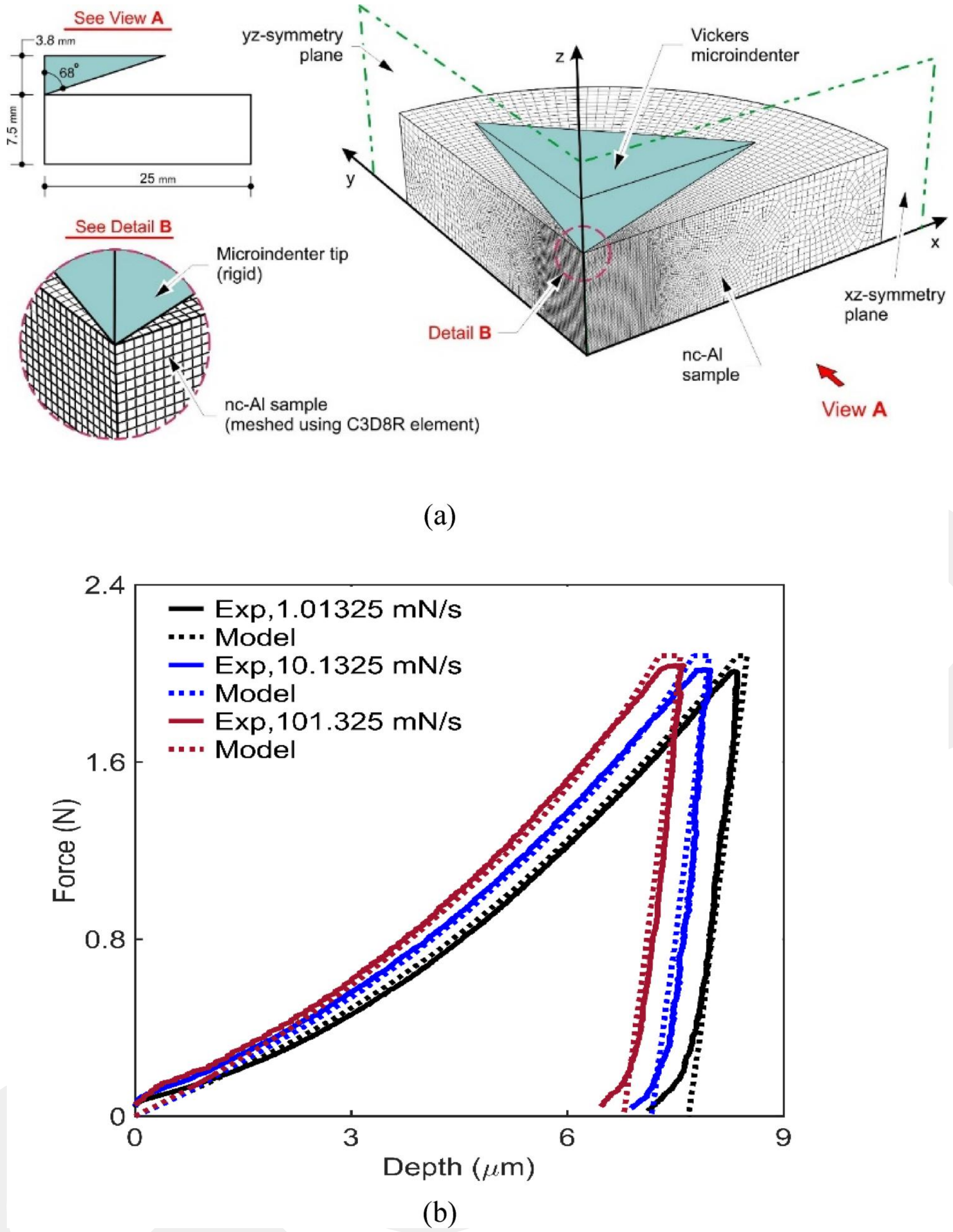

Figure 18. (a) Numerical model used for finite element simulation of Vickers microindentation test, and (b) comparison of finite element simulation results with experimentally-obtained data for nc-Al at loading rates of 1.01325 mN/s, 10.1325 mN/s, and 101.325 mN/s.

Figure 18b demonstrates the numerical predictions obtained from the finite element simulations using the aforementioned numerical model. The simulations were conducted for three representative loading rates of 1.01325 mN/s, 10.1325 mN/s, and 101.325 mN/s. The numerical results are compared with the physical experimental data from the experimental setup established in Section 2.4. From Figure 18b, we can see that the proposed model and its computational implementation can capture the actual applied force-depth response obtained from the Vickers microindentation test for the nc-Al to good accord, and the present theory and its FEM implementation can also rigorously model the rate dependence feature of the nc-Al metal observed from the microindentation test.

4. Conclusions

This work has presented a new synthesizing process for fabricating high-performance nanocrystalline aluminum with an optimal strength-to-ductility ratio using an in-situ hot extrusion-based technique. Various comprehensive mechanical and microstructural investigations on synthesized nanocrystalline aluminum samples indicate a substantial increase in ultimate tensile strength and hardness compared to the conventional coarse grained commercial pure aluminum due to the marked grain refinement to the nanoscale induced by mechanical milling. To our knowledge, achieving such a compromise between mechanical characteristics and ductility has not previously been possible by established synthesizing processes. This new technique demonstrated potential for general applicability to fabricate bulk nanostructured metals.

Furthermore, a constitutive modeling approach has been proposed using a continuum-scale isotropic rate-dependent plasticity model. The constitutive equations have been computationally implemented into Abaqus/Explicit package *via* a user defined material subroutine. The constitutive material parameters have been efficiently calibrated using a curve-fitting-based procedure. For validation purposes, a diverse set of numerical results for simple compression/tension and the Vickers microidentation test have been compared with the experimental data obtained for the synthesized nanocrystalline aluminum. It has been demonstrated that the present approach can successfully reflect the mechanical response of the nc-Al materials, which constitute a foundation for computational design and analysis of macroscale components made of nc-Al materials. As future work, the fatigue behavior of nc-Al materials can be investigated experimentally and theoretically using a microplasticity-based constitutive model [69–71], and the fracture of these materials can also be modeled in a finite-element setting using the element failure/deletion method as a first-cut approach [72].

Disclosure statement

No potential conflict of interest was reported by the author(s).

Funding

S.D., A.M., M.G., and P.T. sincerely acknowledge the financial support from ASEAN-Indian Science and Technology Development Fund (AISTDF), DST, Govt. of India, under Grant No. IMRC/AISTDF/R&D/P-14/2018. F.M. acknowledges the partial support provided by the AGÜ foundation.

References

[1] A. Mallick, S. Vedantam, and L. Lu, Grain size dependent tensile behavior of Mg-3% Al alloy at elevated temperatures, Mater. Sci. Eng. A., vol. 515, no. 1–2, pp. 14–18, Jul. 2009. DOI: 10.1016/j.msea.2009.03.002.

[2] X. Peng, M. Yu, and Y. Liu, Effect of nanotwin and dislocation pileup at twin boundary on dislocation emission from an interfacial collinear crack tip in nanocrystalline bimaterials, Mech. Adv. Mater. Struct., vol. 27, no. 12, pp. 965–974, Jun. 2020. DOI: 10.1080/15376494.2018.1502851.

[3] S. Whalen, M. Olszta, C. Roach, J. Darsell, D. Graff, Md. Reza-E-Rabby, T. Roosendaal, W. Daye, T. Pelletiers, S. Mathaudhu, and N. Overman, High ductility aluminum alloy made from powder by friction extrusion, Materialia., vol. 6, pp. 100260, Jun. 2019. DOI: 10.1016/j.mtla.2019.100260.

[4] Y.S. Han, and V. Tomar, An investigation into the influence of grain boundary misorientation on the tensile strength of SiC bicrystals, Mech. Adv. Mater. Struct., vol. 23, no. 5, pp. 494–502, May 2016. DOI: 10.1080/15376494.2014.984094.

[5] L. Shen, and Z. Chen, Loading history effect on size-dependent shear strength of pure and nitrogen-doped ultrananocrystalline diamond, Mech. Adv. Mater. Struct., vol. 16, no. 7, pp. 504–515, Oct. 2009. DOI: 10.1080/15376490903133244.

[6] A.K. Kushwaha, R. Maccione, M. John, S. Lanka, M. Misra, and P.L. Menezes, Influence of cryomilling on crystallite size of aluminum powder and spark plasma sintered component, Nanomaterials., vol. 12, no. 3, pp. 551, Feb. 2022. DOI: 10.3390/nano12030551.

[7] J.K. Rana, D. Sivaprahasam, K.S. Raju, and V.S. Sarma, Microstructure and mechanical properties of nanocrystalline high-strength Al-Mg-Si (AA6061) alloy by high-energy ball milling and spark plasma sintering, Mater. Sci. Eng. A., vol. 527, no. 1–2, pp. 292–296, Dec. 2009. DOI: 10.1016/j.msea.2009.08.041.

[8] A.S. Khan, Y.S. Suh, X. Chen, L. Takacs, and H. Zhang, Nanocrystalline aluminum and iron: mechanical behavior at quasi-static and high strain rates, and constitutive modeling, Int. J. Plast., vol. 22, no. 2, pp. 195–209, Feb. 2006. DOI: 10.1016/j.ijplas.2004.07.008.

[9] H. Kuleyin, R. Gümruk, H. Yanar, M. Demirtaş, and G. Pürçek, The mechanical compression performance of ultra-fine-grained stainless steel pyramidal lattice core, Mech. Adv. Mater. Struct., vol. 28, no. 10, pp. 1073–1078, May 2021. DOI: 10.1080/15376494.2019.1631413.

[10] G. Nurislamova, X. Sauvage, M. Murashkin, R. Islamgaliev, and R. Valiev, Nanostructure and related mechanical properties of an Al-Mg-Si alloy processed by severe plastic deformation, Philos. Mag. Lett., vol. 88, no. 6, pp. 459–466, Jun. 2008. DOI: 10.1080/09500830802186938.

[11] D. Orlov, N. Kamikawa, and N. Tsuji, High pressure torsion to refine grains in pure aluminum up to saturation: mechanisms of structure evolution and their dependence on strain, Philos. Mag., vol. 92, no. 18, pp. 2329–2350, Jun. 2012. DOI: 10.1080/14786435.2012.671548.

[12] J. Oh, S. Park, H.J. Bae, S. Son, H.S. Kim, J.B. Seol, H. Sung, and J.G. Kim, Mechanical properties and microstructural evolution of high-pressure torsion-processed Al7075 alloy at elevated temperatures, Mater. Sci. Eng. A., vol. 835, pp. 142692, Feb. 2022. DOI: 10.1016/j.msea.2022.142692.

[13] K.M. Agarwal, R.K. Tyagi, V. Choubey, and K.K. Saxena, Mechanical behaviour of Aluminium Alloy AA6063 processed through ECAP with optimum die design parameters, Adv. Mater. Process. Technol., vol. 8, no. 2, pp. 1901–1915, Apr. 2022. DOI: 10.1080/2374068X.2021.1878705.

[14] T. Khelfa, R. Lachhab, H. Azzeddine, Z. Chen, J.A. Muñoz, J.M. Cabrera-Marrero, F. Brisset, A.-L. Helbert, T. Baudin, and M. Khitouni, Effect of ECAP and subsequent annealing on microstructure, texture, and microhardness of an AA6060 aluminum alloy, J. Mater. Eng. Perform., vol. 30, pp. 1–18, Nov. 2021. DOI: 10.1007/s11665-021-06404-w.

[15] T. Tański, P. Snopiński, and W. Borek, Strength and structure of AlMg$_3$ alloy after ECAP and post-ECAP processing, Mater. Manuf. Processes., vol. 32, no. 12, pp. 1368–1374, Sep. 2017. DOI: 10.1080/10426914.2016.1257131.

[16] J. May, H.W. Höppel, and M. Göken, Strain rate sensitivity of ultrafine-grained aluminium processed by severe plastic deformation, Scr. Mater., vol. 53, no. 2, pp. 189–194, Jul. 2005. DOI: 10.1016/j.scriptamat.2005.03.043.

[17] J. Su, Z.-B. Tang, C.-X. Wang, T. Ye, T. Suo, and Y.-L. Li, Compressive behavior and deformation kinetics of ultrafine-grained aluminum processed by equal channel angular pressing, Int. J. Smart Nano Mater., vol. 8, no. 1, pp. 56–77, Jan. 2017. DOI: 10.1080/19475411.2017.1300201.

[18] I. Sabirov, Y. Estrin, M.R. Barnett, I. Timokhina, and P.D. Hodgson, Enhanced tensile ductility of an ultra-fine-grained aluminum alloy, Scr. Mater., vol. 58, no. 3, pp. 163–166, Feb. 2008. DOI: 10.1016/j.scriptamat.2007.09.057.

[19] M. Alvand, M. Naseri, E. Borhani, and H. Abdollah-Pour, Nano/ultrafine-grained AA2024 alloy processed by accumulative roll bonding: a study of microstructure, deformation texture, and mechanical properties, J. Alloys Compd., vol. 712, pp. 517–525, Jul. 2017. DOI: 10.1016/j.jallcom.2017.04.117.

[20] M.R. Morovvati, and B.M. Dariani, The effect of annealing on the formability of aluminum 1200 after accumulative roll bonding, J. Manuf. Process., vol. 30, pp. 241–254, Dec. 2017. DOI: 10.1016/j.jmapro.2017.09.013.

[21] A. Böhner, V. Maier, K. Durst, H.W. Höppel, and M. Göken, Macro- and nanomechanical properties and strain rate sensitivity of accumulative roll-bonded and equal channel angular pressed ultrafine-grained materials, Adv. Eng. Mater., vol. 13, no. 4, pp. 251–255, Apr. 2011. DOI: 10.1002/adem.201000270.

[22] H.L. Yu, C. Lu, A.K. Tieu, and C. Kong, Fabrication of nanostructured aluminum sheets using four-layer accumulative roll bonding, Mater. Manuf. Processes., vol. 29, no. 4, pp. 448–453, Apr. 2014. DOI: 10.1080/10426914.2013.872259.

[23] J.Q. Su, T.W. Nelson, and C.J. Sterling, Grain refinement of aluminum alloys by friction stir processing, Philos. Mag., vol. 86, no. 1, pp. 1–24, Jan. 2006. DOI: 10.1080/14786430500267745.

[24] Z.Y. Ma, A.H. Feng, D.L. Chen, and J. Shen, Recent advances in friction stir welding/processing of aluminum alloys: microstructural evolution and mechanical properties, Crit. Rev. Solid State Mater. Sci., vol. 43, no. 4, pp. 269–333, Jul. 2018. DOI: 10.1080/10408436.2017.1358145.

[25] J.-Q. Su, T.W. Nelson, and C.J. Sterling, Friction stir processing of large-area bulk ultrafine-grained aluminum alloys, Scr. Mater., vol. 52, no. 2, pp. 135–140, Jan. 2005. DOI: 10.1016/j.scriptamat.2004.09.014.

[26] C. Wang, F. Li, L. Wang, and H. Qiao, Review on modified and novel techniques of severe plastic deformation, Sci. China Technol. Sci., vol. 55, no. 9, pp. 2377–2390, Sep. 2012. DOI: 10.1007/s11431-012-4954-y.

[27] E. Salur, A. Aslan, M. Kuntoğlu, and M. Acarer, Effect of ball milling time on the structural characteristics and mechanical properties of nano-sized Y_2O_3 particle-reinforced aluminum matrix composites produced by powder metallurgy route, Adv. Powder Technol., vol. 32, no. 10, pp. 3826–3844, Oct. 2021. DOI: 10.1016/j.apt.2021.08.031.

[28] Z.-F. Liu, Z.-H. Zhang, J.-F. Lu, A.V. Korznikov, E. Korznikova, and F.-C. Wang, Effect of sintering temperature on microstructures and mechanical properties of spark plasma sintered nanocrystalline aluminum, Mater. & Design., vol. 64, pp. 625–630, Dec. 2014. DOI: 10.1016/j.matdes.2014.08.030.

[29] J. Christudasjustus, C.S. Witharamage, G. Walunj, T. Borkar, and R.K. Gupta, The influence of spark plasma sintering temperatures on the microstructure, hardness, and elastic modulus of the nanocrystalline Al-xV alloys produced by high-energy ball milling, J. Mater. Sci. Technol., vol. 122, pp. 68–76, Sep. 2022. DOI: 10.1016/j.jmst.2022.02.008.

[30] C.S. Vidyasagar, and D.B. Karunakar, Effect of spark plasma sintering and reinforcements on the formation of ultra-fine and nanograins in AA2024-TiB_2-Y hybrid composites, Prog. Nat. Sci. Mater. Int., vol. 32, no. 1, pp. 79–86, Feb. 2022. DOI: 10.1016/j.pnsc.2021.07.001.

[31] B.Q. Han, and E.J. Lavernia, Enhanced tensile ductility in a nanostructured Al-7.5% Mg alloy, Mater. Sci. Technol., vol. 21, no. 7, pp. 855–860, Jul. 2005. DOI: 10.1179/174328405X47618.

[32] R.W. Hayes, D. Witkin, F. Zhou, and E.J. Lavernia, Deformation and activation volumes of cryomilled ultrafine-grained aluminum, Acta Mater., vol. 52, no. 14, pp. 4259–4271, Aug. 2004. DOI: 10.1016/j.actamat.2004.05.042.

[33] F. Tang, C.P. Liao, B. Ahn, S.R. Nutt, and J.M. Schoenung, Thermal stability in nanostructured Al-5083/SiC_p composites fabricated by cryomilling, Powder Metall., vol. 50, no. 4, pp. 307–312, Dec. 2007. DOI: 10.1179/174329007X189630.

[34] T.A. Latynina, A.M. Mavlyutov, M.Y. Murashkin, R.Z. Valiev, and T.S. Orlova, The effect of hardening by annealing in ultrafine-grained Al–0.4 Zr alloy: influence of Zr microadditives, Philos. Mag., vol. 99, no. 19, pp. 2424–2443, Oct. 2019. DOI: 10.1080/14786435.2019.1631501.

[35] M.N. Borse, M. Manokaran, S.G. Yebaji, S. Chopra, A. Sourav, B. Majumdar, A. Babu, and S. Thangaraju, Development and characterization of a novel Y-Ti-O based aluminum nano-composite processed by high-energy ball-milling and spark plasma sintering, Mater. Charact., vol. 190, pp. 112013, Aug. 2022. DOI: 10.1016/j.matchar.2022.112013.

[36] A.K. Kushwaha, M. Misra, and P.L. Menezes, Manufacturing bulk nanocrystalline Al-3Mg components using cryomilling and spark plasma sintering, Nanomaterials., vol. 12, no. 20, pp. 3618, Oct. 2022. DOI: 10.3390/nano12203618.

[37] L. Cao, Y. Xie, Y. Luo, J. Liang, J. Wang, D. Zhang, and L. Wang, Effects of annealing and extrusion on the microstructure and tensile properties of ultrafine-grained Al fabricated by spark plasma sintering, Powder Metall., vol. 64, no. 5, pp. 412–424, Oct. 2021. DOI: 10.1080/00325899.2021.1928814.

[38] B.Q. Han, E.J. Lavernia, and F.A. Mohamed, Tension and compression of bulk Al-7.5 wt% Mg alloy, Philos. Mag. Lett., vol. 83, no. 2, pp. 89–96, Jan. 2003. DOI: 10.1080/0950083021000048154.

[39] L. Tan, Z. Wang, Y. Li, Y. Liu, and F. Liu, Strengthening the bimodal-grained powder metallurgy ferritic steels with Cu addition by aging hardening, Mater. Sci. Eng. A., vol. 800, pp. 140312, Jan. 2021. DOI: 10.1016/j.msea.2020.140312.

[40] H.J. Choi, S.W. Lee, J.S. Park, and D.H. Bae, Tensile behavior of bulk nanocrystalline aluminum synthesized by hot extrusion of ball-milled powders, Scripta Mater., vol. 59, no. 10, pp. 1123–1126, Nov. 2008. DOI: 10.1016/j.scriptamat.2008.07.030.

[41] P. Verma, R. Saha, and D. Chaira, Waste steel scrap to nanostructured powder and superior compact through powder metallurgy: powder generation, processing, and characterization, Powder Technol., vol. 326, pp. 159–167, Feb. 2018. DOI: 10.1016/j.powtec.2017.11.061.

[42] A. Hua, Y. Su, Y. Cai, X. Wang, K. Liu, H. Cao, D. Zhang, and Q. Ouyang, Fabrication, microstructure characterization, and mechanical properties of B_4C microparticles and SiC nanowires hybrid reinforced aluminum matrix composites, Mater. Charact., vol. 193, pp. 112243, Nov. 2022. DOI: 10.1016/j.matchar.2022.112243.

[43] A. El-Ghazaly, G. Anis, and H.G. Salem, Effect of graphene addition on the mechanical and tribological behavior of nanostructured AA2124 self-lubricating metal matrix composite, Compos. Part A: Appl. Sci. Manuf., vol. 95, pp. 325–336, Apr. 2017. DOI: 10.1016/j.compositesa.2017.02.006.

[44] R. Xu, Z. Tan, D. Xiong, G. Fan, Q. Guo, J. Zhang, Y. Su, Z. Li, and D. Zhang, Balanced strength and ductility in CNT/Al composites achieved by flake powder metallurgy via shift-speed ball milling, Compos. Part A: Appl. Sci. Manuf., vol. 96, pp. 57–66, May 2017. DOI: 10.1016/j.compositesa.2017.02.017.

[45] Y. Jiang, Z. Tan, R. Xu, G. Fan, D.-B. Xiong, Q. Guo, Y. Su, Z. Li, and D. Zhang, Tailoring the structure and mechanical properties of graphene nanosheet/aluminum composites by flake powder metallurgy via shift-speed ball milling, Compos. Part A: Appl. Sci. Manuf., vol. 111, pp. 73–82, Aug. 2018. DOI: 10.1016/j.compositesa.2018.05.022.

[46] V. Yamakov, D. Wolf, S.R. Phillpot, A.K. Mukherjee, and H. Gleiter, Dislocation processes in the deformation of nanocrystalline aluminium by molecular-dynamics simulation, Nat. Mater., vol. 1, no. 1, pp. 45–48, Sep. 2002. DOI: 10.1038/nmat700.

[47] M. Nikfar, E. Taati, and M. Asghari, On the theoretical and molecular dynamic methods for natural frequencies of multilayer graphene nanosheets incorporating nonlocality and interlayer shear effects, Mech. Adv. Mater. Struct., vol. 29, no. 20, pp. 2873–2883, Jul. 2022. DOI: 10.1080/15376494.2021.1880675.

[48] K. Kadau, P.S. Lomdahl, B.L. Holian, T.C. Germann, D. Kadau, P. Entel, D.E. Wolf, M. Kreth, and F. Westerhoff, Molecular-dynamics study of mechanical deformation in nano-crystalline aluminum, Metall. Mater. Trans. A., vol. 35, no. 9, pp. 2719–2723, Sep. 2004. DOI: 10.1007/s11661-004-0217-2.

[49] Q. Han, and X. Yi, High pressure-induced elimination of grain size softening in nanocrystalline metals: grain boundary strengthening overwhelming reduction of intragranular dislocation storage ability, Int. J. Plasticity., vol. 153, pp. 103261, Jun. 2022. DOI: 10.1016/j.ijplas.2022.103261.

[50] A.S. Khan, and H. Zhang, Mechanically alloyed nanocrystalline iron and copper mixture: behavior and constitutive modeling over

a wide range of strain rates, Int. J. Plasticity., vol. 16, no. 12, pp. 1477–1492, Jan. 2000. DOI: 10.1016/S0749-6419(00)00024-3.

[51] Q. Zhan, T. Suo, C. Wang, K. Xie, and Z. Tang, Temperature sensitivity and prediction of the mechanical behaviors of ultra-fine-grained aluminum under uniaxial compression, Acta Mech. Solida Sin., vol. 27, no. 4, pp. 373–382, Aug. 2014. DOI: 10.1016/S0894-9166(14)60045-8.

[52] Y. Wei, and L. Anand, A constitutive model for powder-processed nanocrystalline metals, Acta Mater., vol. 55, no. 3, pp. 921–931, Feb. 2007. DOI: 10.1016/j.actamat.2006.09.014.

[53] M. Rijesh, M.S. Sreekanth, A. Deepak, K. Dev, and A.O. Surendranathan, Effect of milling time on production of aluminium nanoparticle by high energy ball milling, Int. J. Mech. Eng. Technol., vol. 9, no. 8, pp. 646–652, Aug. 2018.

[54] H. Abdoli, M. Ghanbari, and S. Baghshahi, Thermal stability of nanostructured aluminum powder synthesized by high-energy milling, Mater. Sci. Eng. A., vol. 528, no. 22–23, pp. 6702–6707, Aug. 2011. DOI: 10.1016/j.msea.2011.05.057.

[55] H. Geng, X. Zhang, Y. Wang, Z. Wang, and Y. Zhang, Warm and hot stamping of high-strength aluminum alloy sheets using contact heating, Mech. Adv. Mater. Struct., pp. 1–10, Nov. 2022. DOI: 10.1080/15376494.2022.2145534.

[56] K. Morsi, and A. Esawi, Effect of mechanical alloying time and carbon nanotube (CNT) content on the evolution of aluminum (Al)–CNT composite powders, J. Mater. Sci., vol. 42, no. 13, pp. 4954–4959, Jul. 2007. DOI: 10.1007/s10853-006-0699-y.

[57] S.J. Kim, H.W. Jung, M.W. Lee, Y.J. Kim, Y.H. Huh, and J.H. Park, Heat treatment effects on mechanical properties of Ni–Co alloy thin films, Mech. Adv. Mater. Struct., vol. 26, no. 19, pp. 1589–1595, Oct. 2019. DOI: 10.1080/15376494.2018.1444217.

[58] S. Varam, K.V. Rajulapati, and K.B.S. Rao, Strain rate sensitivity studies on bulk nanocrystalline aluminium by nanoindentation, J. Alloys Compd., vol. 585, pp. 795–799, Feb. 2014. DOI: 10.1016/j.jallcom.2013.09.116.

[59] S.I. Ahmed, K.A. Mkhoyan, and K.M. Youssef, The activation of deformation mechanisms for improved tensile properties in nanocrystalline aluminum, Mater. Sci. Eng. A., vol. 777, pp. 139069, Mar. 2020. DOI: 10.1016/j.msea.2020.139069.

[60] M.R. Akbarpour, F.S. Torknik, and S.A. Manafi, Enhanced compressive strength of nanostructured aluminum reinforced with SiC nanoparticles and investigation of strengthening mechanisms and fracture behavior, J. Materi. Eng. Perform., vol. 26, no. 10, pp. 4902–4909, Oct. 2017. DOI: 10.1007/s11665-017-2871-8.

[61] M. Jafari, M.H. Enayati, M.H. Abbasi, and F. Karimzadeh, Compressive and wear behaviors of bulk nanostructured Al2024 alloy, Mater. Des., vol. 31, no. 2, pp. 663–669, Feb. 2010. DOI: 10.1016/j.matdes.2009.08.020.

[62] J.L. Li, Y.C. Xiong, X.D. Wang, S.J. Yan, C. Yang, W.W. He, J.Z. Chen, S.Q. Wang, X.Y. Zhang, and S.L. Dai, Microstructure and tensile properties of bulk nanostructured aluminum/graphene composites prepared via cryomilling, Mater. Sci. Eng. A., vol. 626, pp. 400–405, Feb. 2015. DOI: 10.1016/j.msea.2014.12.102.

[63] H.M. Ledbetter, and R.P. Reed, Elastic properties of metals and alloys, I. Iron, nickel, and iron-nickel alloys, J. Phys. Chem. Ref. Data., vol. 2, no. 3, pp. 531–618, Jul. 1973. DOI: 10.1063/1.3253127.

[64] A.S. Shedbale, I.V. Singh, B.K. Mishra, and K. Sharma, Evaluation of mechanical properties using spherical ball indentation and coupled finite element–element-free Galerkin approach, Mech. Adv. Mater. Struct., vol. 23, no. 7, pp. 832–843, Jul. 2016. DOI: 10.1080/15376494.2015.1029171.

[65] A.S. Shedbale, I.V. Singh, and B.K. Mishra, Indentation behavior of metal matrix composites reinforced with arbitrary shape particles using a coupled FE-EFG approach, Mech. Adv. Mater. Struct., vol. 29, no. 25, pp. 4427–4444, Oct. 2022. DOI: 10.1080/15376494.2021.1931580.

[66] J. Qiu, Z. Wang, T. Jin, M. Jiao, X. Li, X. Shu, and F. Yang, Investigation on the indentation mechanical performance of aluminum honeycombs, Mech. Adv. Mater. Struct., vol. 29, no. 18, pp. 2607–2616, Jul. 2022. DOI: 10.1080/15376494.2021.1871792.

[67] Y. Xin, H. Yan, S. Yang, H. Li, and S. Cheng, Experimental study on the indentation of epoxy resin–aluminum honeycomb composite sandwich panel, Mech. Adv. Mater. Struct., vol. 28, no. 9, pp. 904–918, May 2021. DOI: 10.1080/15376494.2019.1605009.

[68] J. Deng, X. Xie, M. Zhang, and N. Liao, Effect of Young's modulus on fracture characteristics of SiCO-SiCN multi-layer films by XFEM simulations of nano-indentation, Mech. Adv. Mater. Struct., vol. 30, no. 16, pp. 3225–3230, Jun. 2023. DOI: 10.1080/15376494.2022.2070806.

[69] F. Mozafari, P. Thamburaja, N. Moslemi, and A. Srinivasa, Finite-element simulation of multi-axial fatigue loading in metals based on a novel experimentally-validated microplastic hysteresis-tracking method, Finite Elem. Anal. Des., vol. 187, pp. 103481, May 2021. DOI: 10.1016/j.finel.2020.103481.

[70] F. Mozafari, and I. Temizer, Computational homogenization of fatigue in additively manufactured microlattice structures, Comput. Mech., vol. 71, no. 2, pp. 367–384, Feb. 2023. DOI: 10.1007/s00466-022-02243-1.

[71] F. Mozafari, P. Thamburaja, A.R. Srinivasa, and N. Moslemi, A rate independent inelasticity model with smooth transition for unifying low-cycle to high-cycle fatigue life prediction, Int. J. Mech. Sci., vol. 159, pp. 325–335, Aug. 2019. DOI: 10.1016/j.ijmecsci.2019.05.017.

[72] K. Sarah, P. Thamburaja, A. Srinivasa, and J.N. Reddy, Numerical simulations of damage and fracture in viscoelastic solids using a nonlocal fracture criterion, Mech. Adv. Mater. Struct., vol. 27, no. 13, pp. 1085–1097, Jul. 2020. DOI: 10.1080/15376494.2020.1716414.